

Master's thesis

Anders Aglen Pedersen

Optimization Based System Identification for the milliAmpere Ferry

Master's thesis in Cybernetics & Robotics

Supervisor: Morten Breivik & Glenn Bitar

June 2019

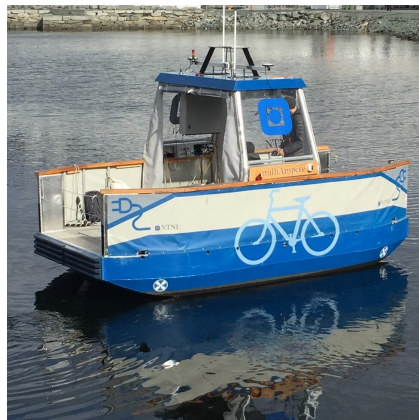
NTNU
Norwegian University of Science and Technology
Faculty of Information Technology and Electrical
Engineering
Department of Engineering Cybernetics



Norwegian University of
Science and Technology

Anders Aglen Pedersen

Optimization Based System Identification for the milliAmpere Ferry



Master's thesis in Cybernetics & Robotics
Supervisor: Morten Breivik & Glenn Bitar
June 2019

Norwegian University of Science and Technology
Faculty of Information Technology and Electrical Engineering
Department of Engineering Cybernetics



Norwegian University of
Science and Technology

Abstract

In this report the findings of experimental tests and system identification of the milliAmpere ferry is presented. The focus of this report is to identify a three degree of freedom ship model that describes the dynamics of the ferry, a thruster model describing propeller and azimuth dynamics and a wind load model describing the wind forces on the ferry. By using optimal control theory, a simulation-based identification method is implemented in Matlab and used to identify the models. The optimal solution is found by defining an optimal control problem and then transcribing it into an nonlinear program and solving it using an interior point method. The identification method is tested and verified by using simulation data obtained from simulating a grey box model. The method is further validated by identifying two dynamic ship models for the milliAmpere ferry, and models for its thrusters. Their performance is verified by cross validation. In addition the wind model is used to find the operating capabilities of the ferry.

Sammendrag

I denne avhandlingen presenteres funnene av eksperimentelle tester og systemidentifikasjon av milliAmpere fergen. Fokuset i denne rapporten er identifisere en skipsmodell med tre frihetsgrader som beskriver fergens dynamikk, en thrustermodell som beskriver propell og asimut-dynamikk og en vindlastmodell som beskriver vindkraften som virker påferga. Ved åbruke optimal kontrollteori implementeres en simuleringsbasert identifiseringsmetode i Matlab og brukes til åidentifisere modellene. Den optimale løsningen er funnet ved ådefinere et optimalt kontrollproblem og ved åtranskribere det til et ikke-lineært program og løse det ved hjelp av interior-point metode. Identifikasjonsmetoden er testet og verifisert ved åbruke simuleringsdata hentet fra en grey-box modell. Metoden er ytterligere validert ved åidentifisere to dynamiske skipsmodeller for ferga, og modeller for dens thrustere. Modellenes ytelse er verifisert ved kryssvalidering.

Preface

This thesis is written as a part of a M.Sc. degree in Cybernetics and Robotics at the Department of Engineering Cybernetics (ITK), Norwegian University of Science and Technology (NTNU). Also, this thesis is a continuation of the work presented in my specialization project (Pedersen, 2018).

First I would like to thank my supervisors Morten Breivik and Glenn Bitar. I am very grateful for the valuable guidance, motivation and support you have given me throughout the work with this thesis. I would also thank my family and my dear Iris which have always been there supporting me throughout these years of studying. In addition, many thanks to Brage Sæther and Emil Thyri, who are also master students at ITK, for the hours together cooperating during the execution of experiments and tests performed on the milliAmpere ferry.

The main goal for this thesis was to identify the dynamics of the milliAmpere ferry and its thruster system. This was done by gathering experimental data through several tests, and using this data in an optimization-based system identification method. The method is a continuation of the work presented in the report (Bitar, 2018) and is implemented using CasADi (v.3.4.5) framework (Andersson et al., 2018) together with Matlab vR2018b. During the semester, the supervisors have contributed with guidance through an hourly follow-up meeting every second week. During these meetings, the progress and other related topics were discussed. Also, I got great help from Glenn in debugging and discussing problems that occurred during the implementation of the system identification method. A lot of time was used to make a good implementation of the identification method and to make it run smoothly.

The foundation for the wind model is a 3D model of the milliAmpere ferry. The surface-area used in the wind-load model is calculated using this 3D model. The 3D model was developed by Glenn Angell and reworked by Professor Adil Rasheed. Both at ITK.

All of the experimental data used in this thesis are gathered from experiments performed in December 2018 and May 2019, except the bollard pull test which was performed by master student Tobias Torben on the 06.06.2018. The details of the experiments in December 2018 can be found in my specialization project (Pedersen, 2018).

Anders Aglen Pedersen
Trondheim, 06 June, 2019

Table of Contents

Abstract	i
Sammendrag	i
Preface	ii
Table of Contents	iv
List of Tables	v
List of Figures	viii
Abbreviations	ix
1 Introduction	1
1.1 Motivation	1
1.2 Related Work	4
1.3 Problem Description	4
1.4 Contributions	5
1.5 Outline	5
2 Background Theory	7
2.1 Ship Model	7
2.2 Thruster Model	11
2.3 Wind Load Model	13
2.4 Model Identification	17
3 System Identification Results	23
3.1 Grey Box Simulation	23
3.1.1 Problem Formulation	24
3.1.2 Identification Results	24
3.1.3 Discussion	27
3.2 milliAmpere	27
3.3 Surge-Decoupled Model for milliAmpere	29
3.3.1 Problem Formulation	30

3.3.2	Identification Results	30
3.3.3	Verification	33
3.3.4	Discussion	35
3.4	Fully-Coupled Model for milliAmpere	35
3.4.1	Problem Formulation	36
3.4.2	Identification Results	36
3.4.3	Verification	38
3.5	Summary & Discussion of the Ship Model Results	40
3.6	Azimuth Model for milliAmpere	42
3.6.1	Problem Formulation	42
3.6.2	Identification Results	43
3.6.3	Verification	43
3.6.4	Discussion	45
3.7	Motor-Speed Model for milliAmpere	46
3.7.1	Problem Formulation	46
3.7.2	Identification Results	47
3.7.3	Verification	48
3.7.4	Discussion	48
3.8	Applications of the Models	50
4	Conclusion & Further Work	53
Bibliography		55
Appendices		57
A	Test Plan for Coupled Tests	59
B	Test Plan for Thrusters	65
C	Bollard Pull Test	69
D	Motor Speed to Thrust	71

List of Tables

2.1	Wind-model parameters for the milliAmpere ferry.	15
3.1	Grey-box model parameter values and estimated parameter values.	27
3.2	milliAmpere spesifications.	28
3.3	Weighting parameters for the surge-decoupled model.	30
3.4	Estimated parameter values for surge-decoupled model.	33
3.5	Weighting parameters for the fully coupled model.	36
3.6	Estimated parameter values for the fully coupled model.	38
3.7	Mean absolute error between estimated and experimental data for velocities with surge-decoupled and fully coupled model. The bottom line shows the objective function value for the solution of the NLP.	41
3.8	Weighting parameters for the azimuth angle model.	42
3.9	Parameters for Azimuth angle model	43
3.10	Weighting parameters for the motorspeed model	47
3.11	Parameters for motor speed model	47

List of Figures

1.1	Illustration of the autonomous, zero-emission container vessel Yara Birkeland. Courtesy of Yara International ASA.	2
1.2	Illustration of the new urban ferry in Trondheim. Courtesy of Petter Mustvedt, Institute of Design, NTNU.	2
1.3	Me, Emil Thyri and Brage Sæther out performing experiments on the milliAmpere, on the 30.05.2019. Courtesy of Brage Sæther.	3
1.4	Map showing the planned route for the autonomous ferry in Trondheim. Courtesy of Egil Eide, NTNU.	3
2.1	Illustration of the different DOFs for a ship. Courtesy of Fossen (2011).	8
2.2	Thruster configuration of the milliAmpere ferry. Courtesy of Torben et al. (2019).	11
2.3	Two azimuth thruster located fore and aft on the milliAmpere ferry. Courtesy of Egil Eide, NTNU.	12
2.4	Experimental data of azimuth angles obtained in (Pedersen, 2018).	13
2.5	Coefficients of lateral and longitudinal resistance, cross-force and rolling mo- ment. Courtesy of Fossen (2011).	15
2.6	Capability plot of the milliAmpere ferry. The line represent maximum relative wind-speed at given angle.	16
2.7	Showing how the integration is performed on the time intervals with step time $h = 0.1$. From (Gros, 2017).	19
3.1	Simulated and estimated velocities after the parameters has been identified for the grey-box model.	25
3.2	Simulated data used in the parameter estimation for the grey-box model. Force and azimuth angle for the two thrusters on the grey-box model.	26
3.3	Me, Emil Thyri and Brage Sæther out performing experiments on the milliAmpere ferry at the harbor basin Brattørkaia on the 30.05.2019. Courtesy of Brage Sæther.	28
3.4	Mapping between rpm and Newton for one thruster, by using tables in Ap- pendix D.	29
3.5	Experimental data and estimated velocities after the parameters have been iden- tified for the surge-decoupled model.	31
3.6	Experimental data used in the parameter estimation for the surge-decoupled model. Thrust and azimuth angle for the two thrusters on the milliAmpere ferry.	32

3.7	Comparison of experimental data and simulated data with the parameters for surge-decoupled model.	34
3.8	Showing the error between experimental and simulated data with the surge-decoupled model.	35
3.9	Experimental data and estimated velocities after the parameters has been identified for the fully coupled model.	37
3.10	Comparison of experimental data and simulated values with the estimated parameters for fully coupled model.	39
3.11	Showing the error between experimental data and simulated with the fully coupled model.	40
3.12	Experimental data and estimated azimuth angles after the parameters has been identified for the azimuth-angle model.	43
3.13	Delay in the azimuth dynamics.	44
3.14	Comparison of experimental data and simulated values for Azimuth angle model.	44
3.15	Error between experimental data and simulated azimuth angle.	45
3.16	Experimental data and estimated motor speeds after the parameters has been identified for the motor-speed model.	48
3.17	Comparison of experimental data and simulated values for motor-speed model.	49
3.18	Error between experimental data and simulated motor speed.	50
3.19	Collision avoidance scenarios. Blue, purple and orange are avoiding the red objects by using different collision-avoidance methods. Courtesy of Thyri (2019).	51

Abbreviations

CO	Center of Object
CG	Center of Gravity
CV	Cross Validation
DOF	Degree of Freedom
EKF	Extended Kalman Filter
GAS	Globally Asymptotically Stable
GPS	Global Positioning System
GNSS	Global Navigation Satellite System
IMU	Inertial Measurement Unit
IPOPT	Interior Point OPTimizer
MPC	Model Predictive Control
NLP	Nonlinear Programming
OCP	Optimal Control Problem
RC	Radio Control
RK4	Runge Kutta 4th-order method
RTK	Real-Time Kinematic
rpm	Revolutions per minute

Introduction

1.1 Motivation

Autonomous ships are gaining interest rapidly in both research and commerce. A lot of money is being invested in this field and the global interest is increasing. Yara with KONGSBERG will be releasing a fully electric container ship in 2020 and it is planned to be fully autonomously operational by 2022 (Skredderberget, 2018). Figure 1.1 shows an illustration of the planned container ship. Rolls-Royce with Finferries recently did a demonstration with a car ferry in Finland, which navigated fully autonomously on its voyage (Rolls-Royce, 2018). Norway is a coastal country with numerous fjords, river and islands which needs crossings and infrastructure related to transportation of goods and people. In 2017 it was approximately 150 ferry connections in Norway, (Bitar, 2017). Also across the world there are numerous urban areas that are built around canals, Figure 1.2 shows an illustration of the small urban passenger ferry concept. A bridge is an expensive investment with high maintenance cost and also an obstacle for marine traffic. Instead by using a fully electric autonomous ferry, flexible urban transportation at low cost and which is more environmentally friendly can be achieved. An accurate mathematical description of a ships dynamics is a necessity in order to make a ship autonomous.

In the city of Trondheim in Norway, it is planned to have a small passenger ferry which will replace the need of a bridge. The Autoferry project, at NTNU, with the vessel milliAmpere, is catching publicity in the media with its goal to make an "on demand" fully autonomous passenger ferry (Stensvold, 2018), (Heggdal, 2016).



Figure 1.1: Illustration of the autonomous, zero-emission container vessel Yara Birkeland. Courtesy of Yara International ASA.



Figure 1.2: Illustration of the new urban ferry in Trondheim. Courtesy of Petter Mustvedt, Institute of Design, NTNU.



Figure 1.3: Me, Emil Thyri and Brage Sæther out performing experiments on the milliAmpere, on the 30.05.2019. Courtesy of Brage Sæther.



Figure 1.4: Map showing the planned route for the autonomous ferry in Trondheim. Courtesy of Egil Eide, NTNU.

The milliAmpere ferry is an autonomous experimental platform with the purpose to be the foundation for the development of technology for a full scale autonomous urban ferry that will

transfer passengers safely over Nidelva in Trondheim. Figure 1.4 shows the planned route for the ferry. For further research on milliAmpere and on its way to become fully autonomous it is necessary to have an accurate mathematical description of its dynamics, to be used for control and simulation purposes.

1.2 Related Work

There exists several methods for identifying model parameters. A common approach is to separate transient elements and steady state elements and use linear regression to find an estimate for the parameter values. In (Eriksen and Breivik, 2017) a non-first-principles model is identified. The model is describing the motion of a high-speed autonomous surface vehicle. The parameter values are found by using weighted linear least squares regression with a regularization term to penalize large parameter values. The model is verified by comparing simulated vessel response and experimental data, and is used in a controller with feed-forward terms. In (Fossen et al., 1996) an offline parallel extended Kalman filter (EKF) algorithm is used to estimate the parameters for a nonlinear dynamic positioned ship model. Three different ship maneuvers are used in a decoupled identification scheme. The identified parameters in the first scheme are used as input in the next scheme until all parameters are identified. The method is verified by implementing and testing it on a supply vessel and comparing the results with experimental data. In (Taylor, 2000) a linear time invariant model of a Burke Class Destroyer is identified by using an online parameter estimator. By using an EKF the linear damping parameters and hydrodynamic coefficients are estimated. Experimental data is generated by conducting maneuvers with a nonlinear model of the ship. The identified model is then validated by using it in model based control design.

1.3 Problem Description

Through experimental work and system identification techniques, an accurate mathematical description of the dynamics of the milliAmpere ferry and its actuators should be developed. In particular the following models must be identified:

- Fully-Coupled ship model
- Surge-decoupled ship model
- Azimuth angle model
- Motorspeed model
- Wind-load model

With these models a foundation for future work regarding prototyping, control and simulation is established. By looking into optimization theory and combining it with classical identification techniques, a tool for system identification should be made, verified and put into use.

1.4 Contributions

A identification method which is based on optimal control theory is implemented and tested on experimental data. The method is able to identify a fully-coupled 3DOF model. The models are well suited to be used for both control and simulation purposes. The dynamic ship models are presented by a fully coupled and a surge-decoupled model. The thruster dynamics is described by a first order model for the propeller dynamics and a sigmoid-function-model representing the azimuth dynamics. The presented models are verified by cross validation. In addition to the ship and thruster dynamics, a wind model based on the ship's projected area is proposed. A total of three experiments (Appendix A and B) are designed and performed on the ferry which provide the experimental data used to identify and verify the models. Also, during the analysis of the experimental data a fault connected to the thruster control system was discovered and corrected.

1.5 Outline

This thesis is organized in the following manner: In Chapter 2 background theory about ship models, thruster models and wind model structures is presented, followed by system identification theory. In Chapter 3, the experimental results from the system identification are presented. Last, in Chapter 4 the conclusion and further work is presented.

Chapter 2

Background Theory

In Section 2.1 the theory behind the ship model is given. Followed by the thruster models in Section 2.2 and wind load model in section 2.3. Finally, system identification theory is presented in Section 2.4.

The notation for marine vessels used in this thesis is adapted from SNAME (1950) and is put together with the vectorial notation by (Fossen, 2011). The resulting ship model is known as the "standard model" for marine control systems design and is well suited for computer implementation and control systems due to useful model properties.

2.1 Ship Model

Mathematical models are used to describe the motion of physical systems under the influence of external forces and is a powerful tool when designing control systems, studying stability properties and for estimation. A 3DOF nonlinear model is proposed together with a thruster model describing the thruster dynamics and a wind model describing environmental forces. The resulting model will be used for simulation, prediction and control. Ship models vary in complexity, and the complexity is dependent on the usage of the model. Different models are used in seakeeping and maneuvering and the number of degrees of freedom is an important aspect. The following model is based on maneuvering theory (Fossen, 2011), and is a nonlinear mass-damper system which describes coupled motion in 3DOF with environmental forces and moments. The milliAmpere ferry is operating in conditions where waves will not have a noticeable impact on the behaviour of the vessel and wave forces are therefore omitted in the model. The following equations form the basis of a dynamical ship model:

$$\dot{\boldsymbol{\eta}} = \mathbf{R}(\psi)\boldsymbol{\nu} \quad (2.1)$$

$$\mathbf{M}\dot{\boldsymbol{\nu}} + \mathbf{C}(\boldsymbol{\nu})\boldsymbol{\nu} + \mathbf{D}(\boldsymbol{\nu})\boldsymbol{\nu} = \boldsymbol{\tau} + \boldsymbol{\tau}_{wind} \quad (2.2)$$

where the pose, velocity and control-action vectors are:

$$\boldsymbol{\eta} = [x, y, \psi]^T \quad (2.3)$$

$$\boldsymbol{\nu} = [u, v, r]^T \quad (2.4)$$

$$\boldsymbol{\tau} = [X, Y, N]^T \quad (2.5)$$

and the rotation matrix:

$$\mathbf{R}(\psi) = \begin{bmatrix} \cos \psi & -\sin \psi & 0 \\ \sin \psi & \cos \psi & 0 \\ 0 & 0 & 1 \end{bmatrix}. \quad (2.6)$$

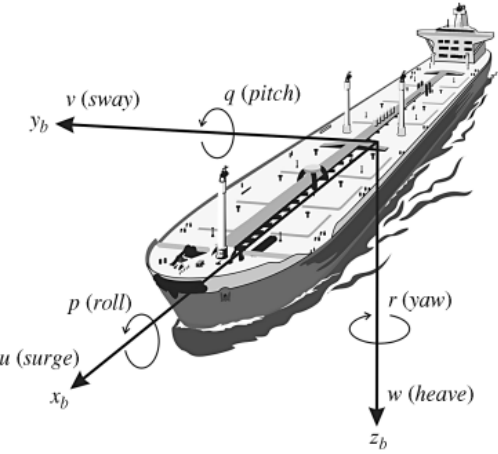


Figure 2.1: Illustration of the different DOFs for a ship. Courtesy of Fossen (2011).

The pose vector $\boldsymbol{\eta}$ is defined in North-East-Down (NED) coordinate system. The x axis points towards true north, y axis towards east and z is pointing downwards. Since milliAmpere will be navigating in a local area, an Earth fixed tangent plane on the surface is used for navigation. This is referred to as flat earth navigation (Fossen, 2011), and one can assume that this is an inertial frame. The linear and angular velocities, $\boldsymbol{\nu}$ are defined in body-fixed reference frame, with o_b in center of object (CO). This is a moving coordinate frame that is fixed to the vessel, where x_b is in the longitudinal axis, y_b the transverse axis and z the normal axis from top to bottom. The 3DOF, that is surge, sway and yaw can is illustrated in Figure 2.1.

A ship that accelerates or decelerates through water must move or deflect some volume of the surrounding water as it moves through it. This is known as hydrodynamic added mass, and the effective mass is considered to be the sum of the body mass and the hydrodynamic added mass. This concerns both the inertia matrix \mathbf{M} and the Coriolis and Centripetal matrix $\mathbf{C}(\boldsymbol{\nu})$, such that:

$$\mathbf{M} = \mathbf{M}_{RB} + \mathbf{M}_A \quad (2.7)$$

$$\mathbf{C}(\boldsymbol{\nu}) = \mathbf{C}_{RB}(\boldsymbol{\nu}) + \mathbf{C}_A(\boldsymbol{\nu}) \quad (2.8)$$

The inertia matrix is positive definite and constant, and is defined as:

$$\mathbf{M} := \begin{bmatrix} m - X_{\dot{u}} & -X_{\dot{v}} & -my_g - X_{\dot{r}} \\ -Y_{\dot{u}} & m - Y_{\dot{v}} & mx_g - Y_{\dot{r}} \\ -my_g - N_{\dot{u}} & mx_g - N_{\dot{v}} & I_z - N_{\dot{r}} \end{bmatrix} \quad (2.9)$$

From a controller and simulation perspective, only the sum of mass and added mass is important, also when identifying parameters experimentally it is difficult to separate inertia parameters from added mass parameters, thus the mass and added mass term can be added together into one value. The inertia matrix \mathbf{M} then becomes

$$\mathbf{M} = \begin{bmatrix} m_{11} & m_{12} & m_{13} \\ m_{21} & m_{22} & m_{23} \\ m_{31} & m_{32} & m_{33} \end{bmatrix}. \quad (2.10)$$

The Coriolis and Centripetal matrix $\mathbf{C}(\boldsymbol{\nu})$ can be expressed as a function of the inertia matrix \mathbf{M} such that it always will be skew-symmetric, that is

$$\mathbf{C}(\boldsymbol{\nu}) = -\mathbf{C}(\boldsymbol{\nu})^T \quad (2.11)$$

where

$$\mathbf{C}(\boldsymbol{\nu}) = \begin{bmatrix} 0 & 0 & c_{13}(\boldsymbol{\nu}) \\ 0 & 0 & c_{23}(\boldsymbol{\nu}) \\ c_{31}(\boldsymbol{\nu}) & c_{32}(\boldsymbol{\nu}) & 0 \end{bmatrix} \quad (2.12)$$

and

$$c_{13}(\boldsymbol{\nu}) = -m_{21}u - m_{22}v - m_{23}r \quad (2.13a)$$

$$c_{23}(\boldsymbol{\nu}) = m_{11}u + m_{12}v + m_{13}r \quad (2.13b)$$

$$c_{31}(\boldsymbol{\nu}) = -c_{13}(\boldsymbol{\nu}) \quad (2.13c)$$

$$c_{32}(\boldsymbol{\nu}) = -c_{23}(\boldsymbol{\nu}). \quad (2.13d)$$

Hydrodynamic damping is defined as the sum of linear viscous damping and nonlinear damping, where the nonlinear damping terms are based on cross-flow drag theory and second-order modulus functions, (Fossen, 2011). It is convenient to write the total hydrodynamic damping as

$$\mathbf{D}(\boldsymbol{\nu}) = \mathbf{D}_L + \mathbf{D}_{NL}(\boldsymbol{\nu}) \quad (2.14)$$

where \mathbf{D}_L is the linear damping matrix and $\mathbf{D}_{NL}(\boldsymbol{\nu})$ the nonlinear damping matrix. The hydrodynamic damping matrix is positive definite and defined as:

$$\mathbf{D}(\boldsymbol{\nu}) = \begin{bmatrix} d_{11}(\boldsymbol{\nu}) & d_{12} & d_{13} \\ d_{21} & d_{22}(\boldsymbol{\nu}) & d_{23}(\boldsymbol{\nu}) \\ d_{31} & d_{32}(\boldsymbol{\nu}) & d_{33}(\boldsymbol{\nu}) \end{bmatrix} \quad (2.15)$$

where

$$d_{11}(\boldsymbol{\nu}) = -X_u - X_{|u|u}|u| - X_{uuu}u^2 \quad (2.16a)$$

$$d_{12} = -X_v \quad (2.16b)$$

$$d_{13} = -X_r \quad (2.16c)$$

$$d_{21} = -Y_u \quad (2.16d)$$

$$d_{22}(\boldsymbol{\nu}) = -Y_v - Y_{|v|v}|v| - Y_{|r|v}|r| - Y_{vvv}v^2 \quad (2.16e)$$

$$d_{23}(\boldsymbol{\nu}) = -Y_r - Y_{|v|r}|v| - Y_{|r|r}|r| \quad (2.16f)$$

$$d_{31} = -N_u \quad (2.16g)$$

$$d_{32}(\boldsymbol{\nu}) = -N_v - N_{|v|v}|v| - N_{|r|v}|r| \quad (2.16h)$$

$$d_{33}(\boldsymbol{\nu}) = -N_r - N_{|v|r}|v| - N_{|r|r}|r| - N_{rrr}r^2. \quad (2.16i)$$

The presented model has properties such as symmetry, skew-symmetry and positive definiteness which are key elements in nonlinear control design and estimation theory. It is also a fully coupled model where it is assumed to be coupled effects in all DOF. However, under the assumption that the origin CO coincides with the CG, that is $[x_g, y_g]^T = \mathbf{0}$, and by looking at symmetry considerations, the expressions for \mathbf{M} , $\mathbf{C}(\boldsymbol{\nu})$ and $\mathbf{D}(\boldsymbol{\nu})$ can be simplified. By using symmetry, it can be assumed that surge is decoupled from sway and yaw and the system equations reduces, such that inertia matrix becomes:

$$\mathbf{M} = \begin{bmatrix} m_{11} & 0 & 0 \\ 0 & m_{22} & m_{23} \\ 0 & m_{32} & m_{33} \end{bmatrix} \quad (2.17)$$

and Coriolis and Centripetal matrix becomes

$$\mathbf{C}(\boldsymbol{\nu}) = \begin{bmatrix} 0 & 0 & c_{13}(\boldsymbol{\nu}) \\ 0 & 0 & c_{23}(\boldsymbol{\nu}) \\ c_{31}(\boldsymbol{\nu}) & c_{32}(\boldsymbol{\nu}) & 0 \end{bmatrix} \quad (2.18)$$

where

$$c_{13}(\boldsymbol{\nu}) = -m_{22}v - m_{23}r \quad (2.19a)$$

$$c_{23}(\boldsymbol{\nu}) = m_{11}u \quad (2.19b)$$

$$c_{31}(\boldsymbol{\nu}) = -c_{13}(\boldsymbol{\nu}) \quad (2.19c)$$

$$c_{32}(\boldsymbol{\nu}) = -c_{23}(\boldsymbol{\nu}). \quad (2.19d)$$

The damping matrix becomes

$$\mathbf{D}(\boldsymbol{\nu}) = \begin{bmatrix} d_{11}(\boldsymbol{\nu}) & 0 & 0 \\ 0 & d_{22}(\boldsymbol{\nu}) & d_{23}(\boldsymbol{\nu}) \\ 0 & d_{32}(\boldsymbol{\nu}) & d_{33}(\boldsymbol{\nu}) \end{bmatrix} \quad (2.20)$$

where the elements in (2.20) are the same as in (2.16a), (2.16e), (2.16f), (2.16h) and (2.16i). Even though there will be coupling terms in all DOF, many of these are considered so small that they can be neglected. However, for small vessels such as milliAmpere coupled effects will have a greater impact on the dynamics than for large vessels. Therefore both the fully coupled system and the surge-decoupled system will be used as candidate models for the system identification method. The resulting models will be verified and their performance compared in Chapter 3

2.2 Thruster Model

To develop a simulation model of the milliAmpere ferry it is important to know the dynamics of the thrusters as the generated force is the main contributor to control forces on a vessel. The actuator system on the milliAmpere ferry consists of two azimuth thrusters, one at the front and one aft. at the vessel. The thruster configuration can be seen in Figure 2.2. The thruster forces are defined by azimuth angles $\boldsymbol{\alpha} = [\alpha_1, \alpha_2]^T$ and thrust force $\mathbf{F} = [F_1, F_2]^T$. The propellers are fixed-pitched, therefore the force components are mainly dependent on the rotational speed of the propeller.

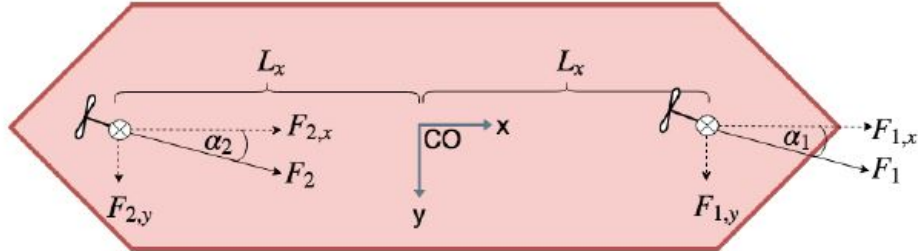


Figure 2.2: Thruster configuration of the milliAmpere ferry. Courtesy of Torben et al. (2019).

Thrust Transformation

The milliAmpere ferry is categorized as a fully-actuated vessel, as it has control inputs in all 3DOF (Fossen, 2011). In the system identification method it is necessary to know the control-action vector $\boldsymbol{\tau}$ in (2.2). The experimental data consist of measurements of azimuth angle and thrust, where the latter is obtained by a mapping between rpm to Newton Appendix D. This does that a transformation is needed. The transformation can be expressed as:

$$\boldsymbol{\tau} = \mathbf{T}(\boldsymbol{\alpha})\mathbf{F} \quad (2.21)$$

where $\mathbf{T}(\boldsymbol{\alpha})$ is the thrust configuration matrix, $\boldsymbol{\alpha}$ is the azimuth angles and \mathbf{F} the thrust force. The control-action vector is obtained by decomposing the thrust forces in \mathbf{F} . The thrust configuration matrix for the milliAmpere then becomes:

$$\mathbf{T}(\alpha) = \begin{bmatrix} \cos \alpha_1 & \cos \alpha_2 \\ \sin \alpha_1 & \sin \alpha_2 \\ L_x \sin \alpha_1 & L_x \sin \alpha_2 \end{bmatrix} \quad (2.22)$$

where L_x is the length from CO to the center of the thrusters.



Figure 2.3: Two azimuth thruster located fore and aft on the milliAmpere ferry. Courtesy of Egil Eide, NTNU.

Azimuth Angle

By looking at experimental data obtained in (Pedersen, 2018), the dynamics for the azimuth angle have a behaviour that is S-shaped. This behaviour is seen in Figure 2.4. The sigmoid-function is a function that is well known for having the characteristic S-shaped curve. The sigmoid function can be expressed as:

$$S(x) = \frac{x}{\sqrt{x^2 + \epsilon^2}}. \quad (2.23)$$

By using (2.23), the dynamics of the azimuth angle can be written as:

$$\dot{\alpha} = K_\alpha \frac{(\alpha_d - \alpha)}{\sqrt{(\alpha_d - \alpha)^2 + \epsilon^2}} \quad (2.24)$$

where α is the azimuth angle, α_d is the desired azimuth angle, $K_\alpha > 0$ is a constant representing the rotational transmission velocity, and ϵ is a tuning parameter to adjust the transient convergence behavior. When saturated, that is $|(\alpha_d - \alpha)| \gg \epsilon$, the slope is defined by K_α .

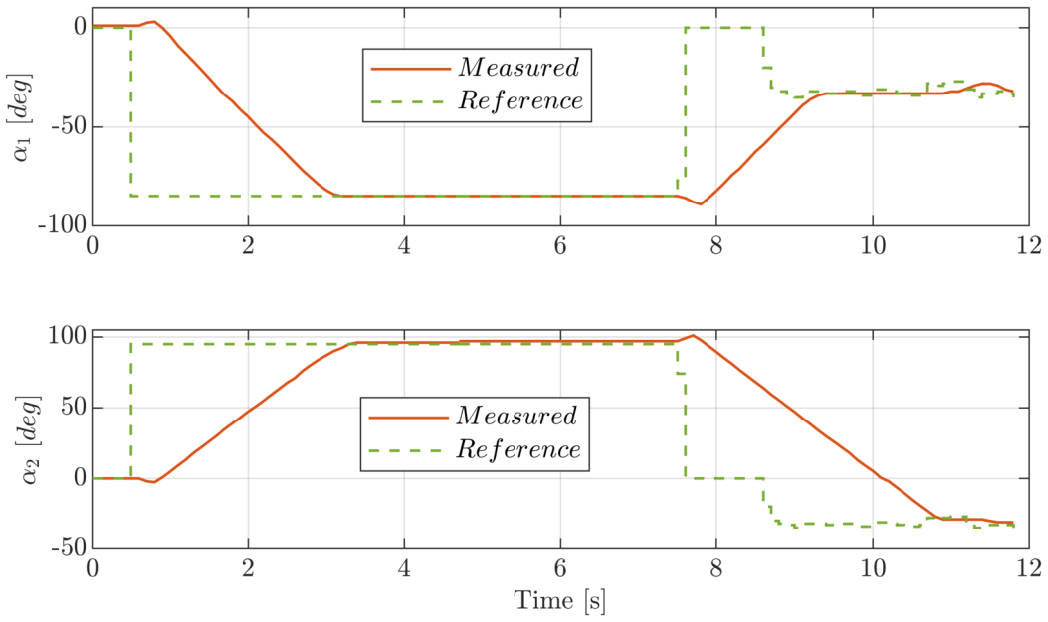


Figure 2.4: Experimental data of azimuth angles obtained in (Pedersen, 2018).

Motor Speed

The propulsion system consists of an electric motor, shaft and propeller. It is typical to assume that the dynamics of the electrical parts of the system are much faster than the propeller shaft dynamics, and therefore it can be neglected. The thrust is provided by the rotating propeller and the modelling of thrust produced by a propeller is a complicated task, mainly because of the numerous thrust losses that occur when a propeller is rotating through a fluid. As stated in (Pivano, 2008) it is difficult to develop a finite-dimensional analytic model from the laws of physics. In this thesis it is focused upon identifying a model that reflects the dynamic behaviour of the actuators of the milliAmpere ferry, that is given by experimental data. For this it is proposed a non-first-principles motor-speed model. This is also encouraged by the experimental data as the obtained motor-speed data has a relatively large sampling time of $h = 0.42s$, which makes it difficult to obtain reliable transient behaviour of the motor-speed dynamics. By experiments a mapping between motor-speed and force is obtained to express the produced thrust. This mapping will also implicitly take the propeller fluid-dynamics, hydrodynamic added mass and other aspects into account. The proposed motor speed model is expressed as

$$\dot{\omega} = K_{\omega}(\omega_d - \omega), \quad (2.25)$$

where ω is rotational the motor speed and ω_d is the desired motor speed. The parameter coefficient $K_{\omega} > 0$ is representing inertia of shaft, electric motor and propeller, hydrodynamic added mass and other physical aspects. This coefficient will be identified experimentally.

2.3 Wind Load Model

During execution of prior experiments on milliAmpere it was experienced that it was very prone to wind forces. As seen in Figure 2.3 milliAmpere has a flat bottom which often gives poor

directional stability, and vulnerable to wind disturbances.

Wind can be defined as the natural movement of air relative to the earth surface. Wind induced loads on a surface are in general time dependent due to natural fluctuations in the air velocity. However, in many situations it is sufficient to know the mean wind force and a simplified model is often enough to be used for simulation and control. The model presented in this section is a coarse wind load model designed to be used for control and simulation purposes of a marine vessel, such that τ_{wind} in (2.2) is known. The wind model is based on the ship's projected area. As described in (Fossen, 2011), wind forces and moment in 3DOF, on a moving marine vessel can be expressed as:

$$\tau_{wind} = q_a \begin{bmatrix} C_X(\gamma_{rw}) A_{Fw} \\ C_Y(\gamma_{rw}) A_{Lw} \\ C_N(\gamma_{rw}) A_{Lw} L_{oa} \end{bmatrix} \quad (2.26)$$

where the dynamic wind pressure is

$$q_a = \frac{1}{2} \rho_{a,T} V_{rw}^2. \quad (2.27)$$

The $\rho_{a,T}$ is the mass density of air at a given temperature T and the relative mean wind speed is defined as:

$$V_{rw} = \sqrt{u_{rw}^2 - v_{rw}^2} \quad (2.28)$$

with the relative velocities defined by vessel and wind velocities such that:

$$u_{rw} = u - u_w \quad (2.29a)$$

$$v_{rw} = v - v_w. \quad (2.29b)$$

The wind direction relative to the vessel is described by the angle of attack which can be calculated using the relative velocities

$$\gamma_{rw} = -\text{atan2}(v_{rw}, u_{rw}) \quad (2.30)$$

The non-dimensional wind coefficients $C_X(\gamma_{rw})$, $C_Y(\gamma_{rw})$ and $C_N(\gamma_{rw})$ in (2.26) are numerically computed using the expressions:

$$C_X(\gamma_w) = -CD_{lAF} \frac{\cos(\gamma_w)}{1 - \frac{\delta}{2}(1 - \frac{CD_l}{CD_t} \sin^2(2\gamma_w))} \quad (2.31a)$$

$$C_Y(\gamma_w) = -CD_t \frac{\sin(\gamma_w)}{1 - \frac{\delta}{2}(1 - \frac{CD_l}{CD_t} \sin^2(2\gamma_w))} \quad (2.31b)$$

$$C_N(\gamma_w) = (\frac{s_L}{L_{oa}} - 0.18(\gamma_w - \frac{\pi}{w}))C_Y(\gamma_w) \quad (2.31c)$$

The longitudinal and lateral resistance coefficients CD_{lAF} , CD_t and cross force coefficient δ are chosen by using row "8. Ferry" in the table presented in Figure 2.5, and

$$CD_l = CD_{lAF}(\gamma_w) \frac{A_{Fw}}{A_{Lw}} \quad (2.32)$$

The frontal and lateral surface area of a vessel are denoted by A_{Fw} and A_{Lw} while L_{oa} is the length over all. For the milliAmpere ferry a 3D computer-aided design model is used to calculate these parameters. These can be found in Table 2.1.

Parameter	Value
A_{Fw}	$2.9m^2$
A_{Lw}	$8.6m^2$
L_{oa}	$5m$
s_L	$0m$

Table 2.1: Wind-model parameters for the milliAmpere ferry.

Type of vessel	CD_t	$CD_{lAF}(0)$	$CD_{lAF}(\pi)$	δ	κ
1. Car carrier	0.95	0.55	0.60	0.80	1.2
2. Cargo vessel, loaded	0.85	0.65	0.55	0.40	1.7
3. Cargo vessel, container on deck	0.85	0.55	0.50	0.40	1.4
4. Container ship, loaded	0.90	0.55	0.55	0.40	1.4
5. Destroyer	0.85	0.60	0.65	0.65	1.1
6. Diving support vessel	0.90	0.60	0.80	0.55	1.7
7. Drilling vessel	1.00	0.70–1.00	0.75–1.10	0.10	1.7
8. Ferry	0.90	0.45	0.50	0.80	1.1
9. Fishing vessel	0.95	0.70	0.70	0.40	1.1
10. Liquefied natural gas tanker	0.70	0.60	0.65	0.50	1.1
11. Offshore supply vessel	0.90	0.55	0.80	0.55	1.2
12. Passenger liner	0.90	0.40	0.40	0.80	1.2
13. Research vessel	0.85	0.55	0.65	0.60	1.4
14. Speed boat	0.90	0.55	0.60	0.60	1.1
15. Tanker, loaded	0.70	0.90	0.55	0.40	3.1
16. Tanker, in ballast	0.70	0.75	0.55	0.40	2.2
17. Tender	0.85	0.55	0.55	0.65	1.1

Figure 2.5: Coefficients of lateral and longitudinal resistance, cross-force and rolling moment. Courtesy of Fossen (2011).

This concludes the wind load model. By using the presented wind model a capability plot is made. A capability plot visualizes the limits of the wind speeds a vessel can operate in. The capability plot for milliAmpere can be seen in Figure 2.6. The capability plot shows that it can handle very high wind speeds directly in surge, but can only handle wind speeds up to $12\frac{m}{s}$ in the range $[45^\circ, 135^\circ]$ and $[225^\circ, 270^\circ]$.

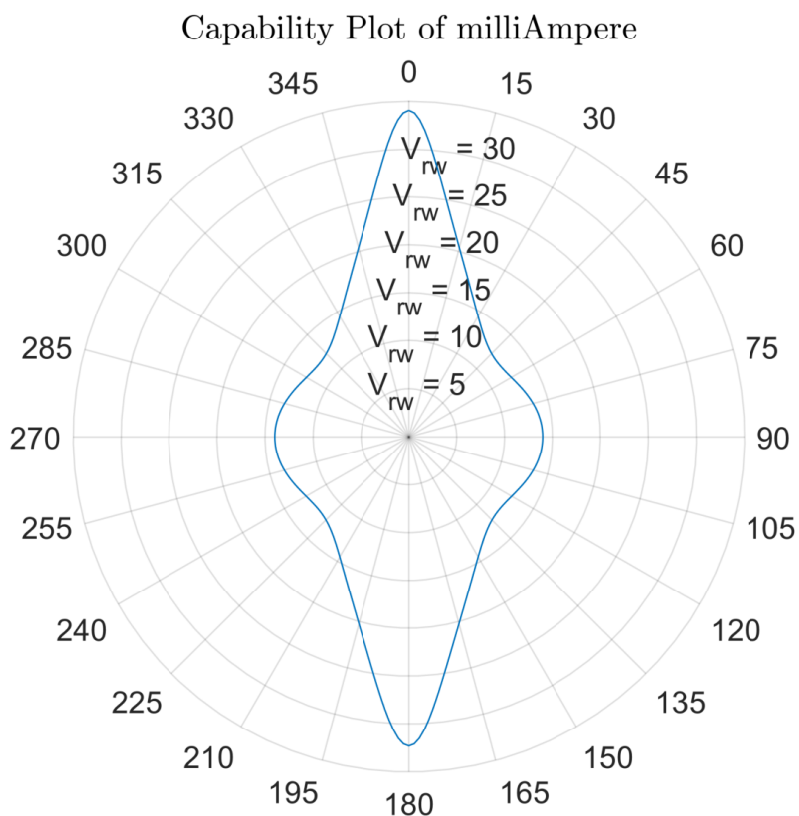


Figure 2.6: Capability plot of the milliAmpere ferry. The line represent maximum relative wind-speed at given angle.

2.4 Model Identification

In this section the background theory for the experiment design and data processing is presented. Followed by the theory for the optimization based system identification method.

Design of Experiments

To be able to get the necessary information about the dynamics of the vessel and thrusters, it is important to have an experiment that is well suited. As described in (Eriksen and Breivik, 2017), a similar structure for a test plan is developed for experiments on milliAmpere. This can be found in Appendix A and Appendix B. The experiments need to produce data that consists of both transient and steady state behaviour of the vessel and thrusters. To be able to produce accurate parameters, the data gathered must be representative of the whole operating space. For the dynamics of the vessel several tests are constructed which gives data of both coupled and non coupled motion. As the diagonal damping terms are of 3rd-order, a minimum of three steady state values must be obtained in each DOF. The commanded input is given in percent and the implemented control-allocation is used to calculate desired angles and motor speed. For the thruster dynamics, separate tests are constructed for the azimuth angles and motor speeds. The azimuth angle is given in degrees, and motorspeed in revolutions per minute (rpm).

Data Extraction

From the experiments, experimental data is collected in datasets. One experiment includes several datasets which are to be used to identify the different models.

When processing the data it was noted that the collected data in the datasets have different sampling times. This will cause problems when they are used together in the identification method. Data for velocity have a sampling time of $h = 0.05$ seconds and data for propeller speed have sampling time of 0.42 seconds, while data of azimuth angle are sampled every 0.1 seconds. By interpolating the data, they are fitted to the sampling time, $h = 0.1$ seconds. Under the implementation and testing of the identification method it was noted that it used relatively long time when identifying the coupled ship model due to the large number of decision variables and model parameters. To lower the calculation cost it was decided to use the sampling time $h = 0.1$ for all datasets by interpolation. The method used for interpolating is Matlab's "linear", which linearly interpolates the values at neighboring grid points. Measurement points outside the domain is evaluated with an extrapolation strategy equal to the one used in interpolation.

Each dataset contains data of velocities $\bar{\nu} = [\bar{u}, \bar{v}, \bar{r}]^T$, rotational velocity for the propellers $\bar{\omega} = [\bar{\omega}_1, \bar{\omega}_2]^T$ and azimuth angles for the thrusters $\bar{\alpha} = [\bar{\alpha}_1, \bar{\alpha}_2]^T$. Note that symbols with a bar, as \bar{x} , indicates that the value is experimentally obtained and not estimated.

Data from multiple experiments are gathered and put in the same set. Datasets for each of the three models are built. As the different models requires different data it is convenient to extract the necessary data into new sets on the form:

$$\mathcal{D}_k = \{(\bar{x}_{10}^T, \bar{x}_{11}^T, \dots, \bar{x}_{1N_1}^T, \bar{x}_{20}^T, \bar{x}_{21}^T, \dots, \bar{x}_{JN_J}^T), \\ (\bar{u}_{10}^T, \bar{u}_{11}^T, \dots, \bar{u}_{1N_1}^T, \bar{u}_{20}^T, \bar{u}_{21}^T, \dots, \bar{u}_{JN_J}^T)\} \quad (2.33)$$

where J is the number of datasets used and N is the length of each dataset. By using (2.33) a set for ship model, azimuth model and motor-speed model is constructed:

$$\mathcal{D}_1 = \{(\bar{\nu}_{10}^T, \bar{\nu}_{11}^T, \dots, \bar{\nu}_{1N_1}^T, \bar{\nu}_{20}^T, \bar{\nu}_{21}^T, \dots, \bar{\nu}_{JN_J}^T), \\ (\bar{\mathbf{u}}_{10}^T, \bar{\mathbf{u}}_{11}^T, \dots, \bar{\mathbf{u}}_{1N_1}^T, \bar{\mathbf{u}}_{20}^T, \bar{\mathbf{u}}_{21}^T, \dots, \bar{\mathbf{u}}_{JN_J}^T)\} \quad (2.34a)$$

$$\mathcal{D}_2 = \{(\bar{\alpha}_{10}^T, \bar{\alpha}_{11}^T, \dots, \bar{\alpha}_{1N_1}^T, \bar{\alpha}_{20}^T, \bar{\alpha}_{21}^T, \dots, \bar{\alpha}_{JN_J}^T), \\ (\bar{\alpha}_{d_{10}}^T, \bar{\alpha}_{d_{11}}^T, \dots, \bar{\alpha}_{d_{JN_1}}^T, \bar{\alpha}_{d_{20}}^T, \bar{\alpha}_{d_{21}}^T, \dots, \bar{\alpha}_{d_{JN_J}}^T)\} \quad (2.34b)$$

$$\mathcal{D}_3 = \{(\bar{\omega}_{10}^T, \bar{\omega}_{11}^T, \dots, \bar{\omega}_{1N_1}^T, \bar{\omega}_{20}^T, \bar{\omega}_{21}^T, \dots, \bar{\omega}_{JN_J}^T), \\ (\bar{\omega}_{d_{10}}^T, \bar{\omega}_{d_{11}}^T, \dots, \bar{\omega}_{d_{JN_1}}^T, \bar{\omega}_{d_{20}}^T, \bar{\omega}_{d_{21}}^T, \dots, \bar{\omega}_{d_{JN_J}}^T)\} \quad (2.34c)$$

where (2.34a) through (2.34c) are the data sets used for the identification of ship model, azimuth model and motor speed model, respectively. Before the data is being used in the identification analysis a wild point filtering is done which gives an error if a wild point is found in one of the datasets. A wild point is defined by that the magnitude of the change is larger than a given value, that is

$$w_k > \delta_{max} \quad (2.35)$$

where

$$w_k := x_{k+1} - x_k, \forall k \in [0, 1, \dots, N-1] \quad (2.36)$$

Problem Formulation

The system identification problem can be formulated in a way that is similar to model predictive control (MPC). By simulating the dynamics of a candidate model at each timestep a dynamic optimization problem is solved. The same problem formulation is being used for the ship and thruster models, therefore a general notation will be used here. The bar notation, \bar{x} , is used for values that comes from experimental data and \mathbf{x} is representing decision variables while the parameter vector \mathbf{P} is representing model parameters that is to be identified. By formulating the problem as an Optimal Control Problem (OCP), it can be expressed as

$$\min_{\mathbf{P}, \mathbf{x}} \quad \int_0^{t_f} L(\mathbf{x}(t), \bar{\mathbf{x}}(t), \mathbf{P}) dt \quad (2.37a)$$

$$s.t \quad \dot{\mathbf{x}}(t) = \mathbf{f}(\mathbf{x}(t), \bar{\mathbf{u}}(t), \mathbf{P}) \quad \forall t \in [0, t_f] \quad (2.37b)$$

$$h(\mathbf{x}(t)) \leq 0 \quad \forall t \in [0, t_f]. \quad (2.37c)$$

$$(2.37d)$$

where the solution is a set of parameters \mathbf{P} that minimizes the objective function, which is the weighted least squares (Hastie, 2009):

$$L(\mathbf{x}(t), \bar{\mathbf{x}}(t), \mathbf{P}) = (\mathbf{x}(t) - \bar{\mathbf{x}}(t))^T \mathbf{W} (\mathbf{x}(t) - \bar{\mathbf{x}}(t)) \quad (2.38)$$

where the weight coefficients $W_{mn} > 0$ such that, $\mathbf{W} = \text{diag}(W_{11}, W_{22}, \dots, W_{mn})$. A problem can be defined as a convex program if the objective function is convex, the equality constraints are linear and inequality constraints concave (Nocedal and Wright, 2006). The objective function (2.38) is convex and has a global minimum at $\mathbf{x} = \bar{\mathbf{x}}$ thus there is a set of \mathbf{P} that gives a global optimal solution. However the equality constraint (2.37b) is nonlinear making this a nonconvex problem. This implies that it exists many local minimums making the solution sensitive for the initial guesses for \mathbf{P} . The initial guesses should therefore be chosen such that the solution converges to a global minimum. The approach used for the initial guess is explained in for the different models in Chapter 3.

Multiple Shooting

To find a solution of the OCP (2.37) a numerical approach is used. By using multiple shooting the OCP is transcribed into an NLP. The key idea of multiple shooting is that the integration function can be made arbitrarily linear by reducing the integration time. By discretizing the input variables \mathbf{u} on the time grid $[t_0, t_1, \dots, t_N]$, the function $f(\mathbf{x}, \bar{\mathbf{u}})$ is integrated on the time intervals $[t_k, t_{k+1}]$. The integrator function then becomes $F(\mathbf{x}_k, \bar{\mathbf{u}}_k)$. This will form a trajectory which is physically meaningful when the shooting gaps are closed, that is

$$F(\mathbf{x}_k, \bar{\mathbf{u}}_k) - \mathbf{x}_{k+1} = 0, \quad k \in [0, 1, \dots, N]. \quad (2.39)$$

It can be seen in Figure 2.7 how the trajectory is forming as the shooting gaps are closing (blue line).

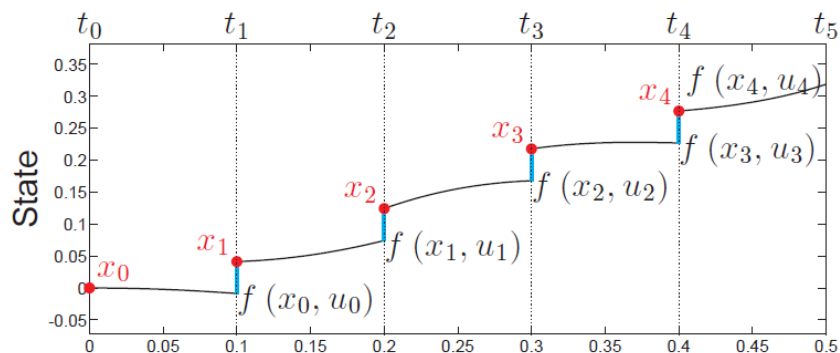


Figure 2.7: Showing how the integration is performed on the time intervals with step time $h = 0.1$. From (Gros, 2017).

The result is a sparse NLP on the form

$$\min_{\mathbf{w}} \phi(\mathbf{w}, \bar{\mathbf{w}}) \quad (2.40a)$$

$$s.t \quad \mathbf{g}(\mathbf{w}) = \mathbf{0} \quad (2.40b)$$

$$h(\mathbf{w}) \leq 0. \quad (2.40c)$$

$$\mathbf{w}_{lb} \leq \mathbf{w} \leq \mathbf{w}_{ub} \quad (2.40d)$$

$$\mathbf{w}(0) = \bar{\mathbf{w}}(0) \quad (2.40e)$$

where the decision vector $\mathbf{w} = [\mathbf{x}_{10}^T, \mathbf{x}_{11}^T, \dots, \mathbf{x}_{1N_1}^T, \mathbf{x}_{20}^T, \mathbf{x}_{21}^T, \dots, \mathbf{x}_{JN_J}^T, \mathbf{P}^T]^T$ contains the decision variables \mathbf{x}_{jk} and model parameters \mathbf{P} . The experimental data vector $\bar{\mathbf{w}}$ is obtained from (2.33). The shooting constraints (2.39) are included in (2.40b) and are integrated with Runge Kutta method of 4th order (RK4), such that

$$\mathbf{x}_{11} = \mathbf{F}(\mathbf{x}_{10}, \bar{\mathbf{u}}_{10}) \quad (2.41)$$

$$g(\mathbf{w}) = \begin{bmatrix} \mathbf{F}(\mathbf{x}_{10}, \bar{\mathbf{u}}_{10}) - \mathbf{x}_{11} \\ \vdots \\ \mathbf{F}(\mathbf{x}_{1N_1-1}, \bar{\mathbf{u}}_{1N_1-1}) - \mathbf{x}_{1N_1} \\ \mathbf{F}(\mathbf{x}_{20}, \bar{\mathbf{u}}_{20}) - \mathbf{x}_{21} \\ \vdots \\ \mathbf{F}(\mathbf{x}_{JN_J-1}, \bar{\mathbf{u}}_{JN_J-1}) - \mathbf{x}_{JN_J} \end{bmatrix} = \mathbf{0}. \quad (2.42)$$

The objective function from (2.38) becomes

$$\phi(\mathbf{w}, \bar{\mathbf{w}}) = \sum_{j=1}^J \sum_{n=1}^{N_j} (\mathbf{x}_{jn} - \bar{\mathbf{x}}_{jn})^T \mathbf{W}_j (\mathbf{x}_{jn} - \bar{\mathbf{x}}_{jn}) \quad (2.43)$$

This concludes the formulation of the identification method. It is implemented using the CasADI (v.3.4.5) framework (Andersson et al., 2018) together with Matlab vR2018b. The NLP is solved using the interior point method Interior Point OPTimizer (IPOPT) (Wächter and Biegler, 2005). The nonlinear solver is an interior point algorithm, and is used with a Eclipse Public License, which is an open source software license. The solution of the NLP provides the optimal set of estimated \mathbf{w} and model parameters \mathbf{P} . The measurement data may be influenced by noise. Noise with zero mean is filtered by the loss function when the size of the data set is large.

Regularization

When an analysis corresponds too closely to a dataset the problem with overfitting can occur. Overfitting is unwanted due to the lack of predictive robustness of the identified model. The predictive abilities of the model gives good results for data used in the analysis but tends to give large prediction errors for unseen data, thus it loses generality. This tends to occur when the ratio between model parameters and data points becomes too small. Regularization introduces a penalty term to the objective function with the purpose to penalize large parameter values.

This results in a more general model that captures the underlying dynamics but not noise and data errors. By introducing a regularization term to the objective function, (2.43) becomes

$$\phi(\mathbf{w}, \bar{\mathbf{w}}) = \sum_{j=1}^J \sum_{n=1}^{N_j} (\mathbf{x}_{jn} - \bar{\mathbf{x}}_{jn})^T \mathbf{W} (\mathbf{x}_{jn} - \bar{\mathbf{x}}_{jn}) + \lambda \mathbf{R}(\mathbf{P}) \quad (2.44)$$

where $\mathbf{R}(\mathbf{P})$ is the L_2 norm $\|\mathbf{P}\|_2$ also known as ridge regression. The regularization weight $\lambda > 0$ is a hyperparameter and is defined by cross validation (CV).

Cross Validation

Cross validation is a widely used method for estimating prediction errors and to validate the performance of a model. By testing the model on datasets not used in the identification process statistical errors like overfitting can be detected. CV can also be used to find the value of hyperparameters. These are parameters that has to be defined before the final parameter estimation is performed. The regularization weight λ is a hyper parameter and can be determined by CV. The principle is to divide available data into a training set and validation set. The training set is used for parameter estimation and the validation set is used to evaluate the loss. By minimizing the loss with respect to λ , the value of λ is defined by the value giving the least loss after all data has been though training and validation set. In sparse data sets it is recommended by Hastie (2009) to use K-Fold CV which splits the data into equal sized parts. A special case of K-fold CV is "leave one out", which evaluates all combinations of leaving one sample for the validation set. This can also be used to verify a model's performance.

Chapter 3

System Identification Results

In this chapter, the theory presented in Chapter 2 is put into use. First a grey box model is identified, and by comparing estimated to actual model parameters the identification method is verified. In Section 3.3 the results of the ship model identification is presented. The results for the thruster dynamics is presented in Section 3.6 and 3.7. By using the identified models and testing them with experimental data not used in the identification part, a cross validation is performed to give an overview of the model's performance.

3.1 Grey Box Simulation

A greybox model is implemented in Matlab using the model parameters presented in (Lingstadaas et al., 2018), shown in Table 3.1. A recap from Chapter 2. The ship model is expressed as

$$\boldsymbol{M}\dot{\boldsymbol{\nu}} + \boldsymbol{C}(\boldsymbol{\nu})\boldsymbol{\nu} + \boldsymbol{D}(\boldsymbol{\nu})\boldsymbol{\nu} = \boldsymbol{\tau} \quad (3.1)$$

with \boldsymbol{M} , $\boldsymbol{C}(\boldsymbol{\nu})$ and $\boldsymbol{D}(\boldsymbol{\nu})$ defined by the surge-decoupled structure given by

$$\boldsymbol{M} = \begin{bmatrix} m_{11} & 0 & 0 \\ 0 & m_{22} & m_{23} \\ 0 & m_{32} & m_{33} \end{bmatrix} \quad (3.2)$$

$$\boldsymbol{C}(\boldsymbol{\nu}) = \begin{bmatrix} 0 & 0 & c_{13}(\boldsymbol{\nu}) \\ 0 & 0 & c_{23}(\boldsymbol{\nu}) \\ c_{31}(\boldsymbol{\nu}) & c_{32}(\boldsymbol{\nu}) & 0 \end{bmatrix} \quad (3.3)$$

$$\boldsymbol{D}(\boldsymbol{\nu}) = \begin{bmatrix} d_{11}(\boldsymbol{\nu}) & 0 & 0 \\ 0 & d_{22}(\boldsymbol{\nu}) & d_{23}(\boldsymbol{\nu}) \\ 0 & d_{32}(\boldsymbol{\nu}) & d_{33}(\boldsymbol{\nu}) \end{bmatrix} \quad (3.4)$$

The grey-box model is implemented with two thrusters located fore and aft, $0.5m$ from CO. The thruster dynamics are ideal with the same control allocation that is used on the milliAmpere ferry. Max thrust per thruster is set to be $100N$. The control allocation is an implementation of the work presented in (Torben et al., 2019).

According to the test plan Appendix A, experiments are simulated with the grey-box model and simulation data is gathered in sets. A total of 15 maneuvers are simulated and the simulation data are created by using a RK4 method. It is also added uniformly distributed noise in the interval $[-0.05, 0.05]$ to the simulation data. By structuring a NLP as in section 2.4 and solving with the IPOPT method a solution is found.

3.1.1 Problem Formulation

By using the NLP as it is defined in (2.40) with the velocities $\boldsymbol{\nu} = [u, v, r]$ and input forces and moment $\bar{\tau} = \mathbf{T}(\bar{\alpha})\bar{\mathbf{F}}$, the problem formulation for the greybox model becomes

$$\min_{\mathbf{w}} \phi(\mathbf{w}, \bar{\mathbf{w}}) \quad (3.5a)$$

$$s.t \quad \mathbf{g}(\mathbf{w}) = \mathbf{0} \quad (3.5b)$$

$$h(\mathbf{w}) \leq 0. \quad (3.5c)$$

$$\mathbf{w}_{lb} \leq \mathbf{w} \leq \mathbf{w}_{ub} \quad (3.5d)$$

$$\mathbf{w}(0) = \bar{\mathbf{w}}(0) \quad (3.5e)$$

where

$$\phi(\mathbf{w}, \bar{\mathbf{w}}) = \sum_{j=1}^J \sum_{n=1}^{N_j} (\boldsymbol{\nu}_{jn} - \bar{\boldsymbol{\nu}}_{jn})^T \mathbf{W}_j (\boldsymbol{\nu}_{jn} - \bar{\boldsymbol{\nu}}_{jn}) + \lambda \mathbf{R}(\mathbf{P}) \quad (3.6a)$$

$$\mathbf{w} = [\boldsymbol{\nu}_{10}^T, \boldsymbol{\nu}_{11}^T, \dots, \boldsymbol{\nu}_{1N}^T, \boldsymbol{\nu}_{20}^T, \boldsymbol{\nu}_{21}^T, \dots, \boldsymbol{\nu}_{JN_J}^T, P^T]^T \quad (3.6b)$$

$$\bar{\mathbf{w}} = [\bar{\boldsymbol{\nu}}_{10}^T, \bar{\boldsymbol{\nu}}_{11}^T, \dots, \bar{\boldsymbol{\nu}}_{1N_1}^T, \bar{\boldsymbol{\nu}}_{20}^T, \bar{\boldsymbol{\nu}}_{21}^T, \dots, \bar{\boldsymbol{\nu}}_{JN_J}^T]^T \quad (3.6c)$$

and the equality constraints

$$g(\mathbf{w}) = \begin{bmatrix} \mathbf{F}(\boldsymbol{\nu}_{10}, \bar{\tau}_{10}) - \boldsymbol{\nu}_{11} \\ \dots \\ \mathbf{F}(\boldsymbol{\nu}_{1N_1-1}, \bar{\tau}_{1N_1-1}) - \boldsymbol{\nu}_{1N_1} \\ \mathbf{F}(\boldsymbol{\nu}_{20}, \bar{\tau}_{20}) - \boldsymbol{\nu}_{21} \\ \dots \\ \mathbf{F}(\boldsymbol{\nu}_{JN_J-1}, \bar{\tau}_{JN_J-1}) - \boldsymbol{\nu}_{JN_J} \end{bmatrix} = \mathbf{0} \quad (3.7)$$

The model parameters to be identified are:

$$\begin{aligned} \mathbf{P} = & [m_{11}, m_{22}, m_{23}, m_{32}, m_{33}, X_u, X_{|u|u}, X_{uuu}, \\ & Y_v, Y_{|v|v}, Y_{vvv}, Y_{|r|r}, Y_r, Y_{|v|r}, Y_{|r|r}, N_v, N_{|v|v}, N_{|r|v}, N_r, N_{|r|r}, N_{rrr}, N_{|v|r}] \end{aligned} \quad (3.8)$$

For the greybox model the weight matrix \mathbf{W} is weighted diagonal ones and hyperparameter $\lambda = 0$.

3.1.2 Identification Results

The simulation data of the grey-box model is gathered in a dataset and used in the identification method. The identification results for the grey-box model are presented in Figure 3.1, showing

the estimated and simulated velocities. The identified parameters are presented in Table 3.1. Figure 3.2 shows the simulated model input.

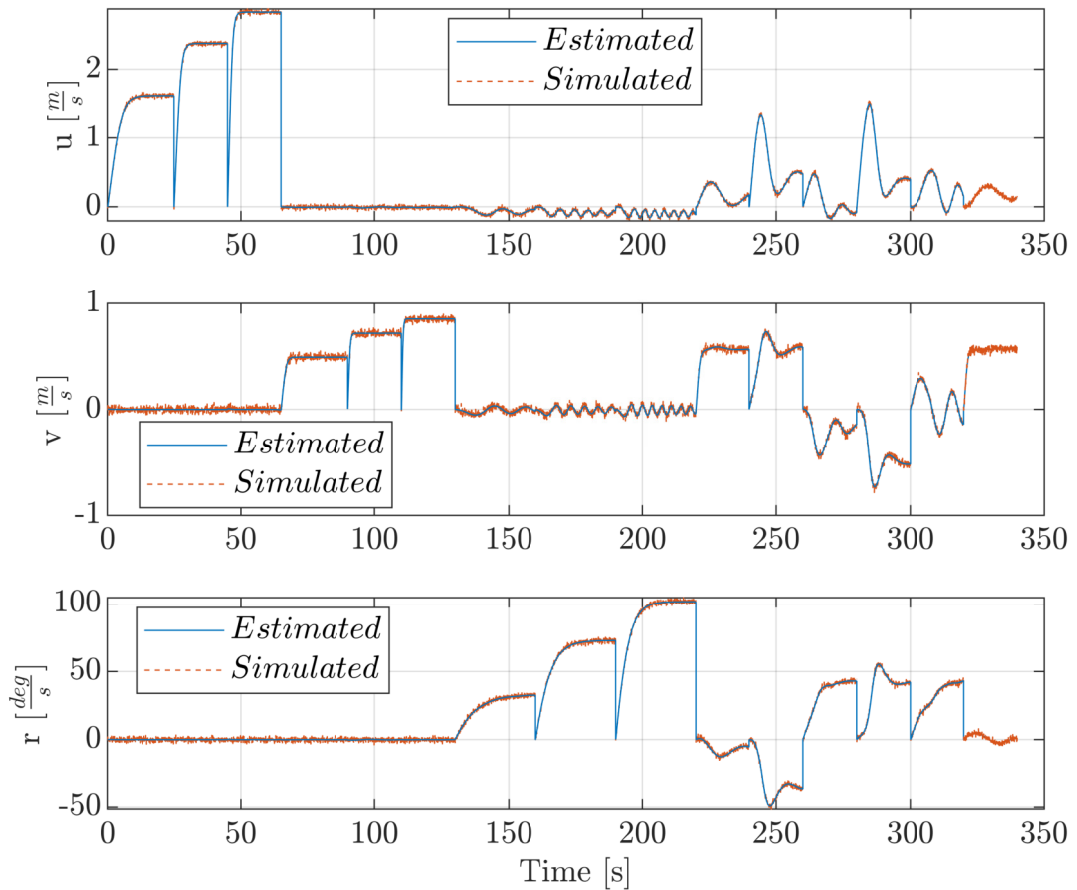


Figure 3.1: Simulated and estimated velocities after the parameters has been identified for the grey-box model.

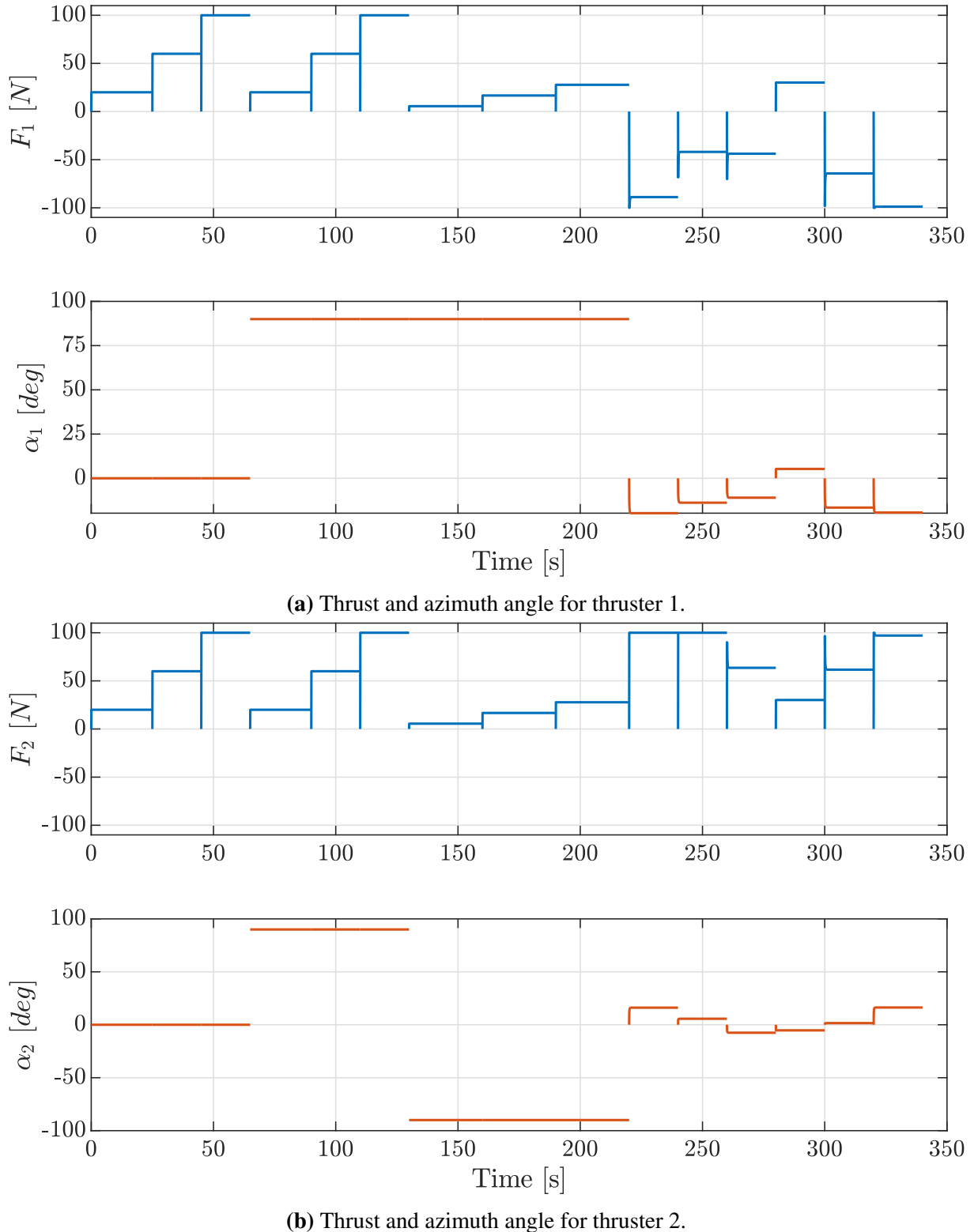


Figure 3.2: Simulated data used in the parameter estimation for the grey-box model. Force and azimuth angle for the two thrusters on the grey-box model.

Parameter	Original Value	Estimated Value	Unit
m_{11}	131.182	131.095	kg
m_{22}	156.810	156.682	kg
m_{23}	0.525	0.457	kg
m_{32}	0.157	0.151	kg
m_{33}	75.967	75.910	kgm^2
X_u	-2.262	-2.379	$\frac{kg}{s}$
$X_{ u u}$	0.000	0.000	$\frac{kg}{s}$
X_{uuu}	-8.557	-8.532	$\frac{kg}{s}$
Y_v	-4.673	-4.317	$\frac{kg}{s}$
$Y_{ v v}$	-0.398	-1.822	$\frac{kg}{s}$
Y_{vvv}	-313.300	-312.217	$\frac{kg}{s}$
$Y_{ r v}$	-0.805	-1.822	$\frac{kg}{s}$
Y_r	-7.250	-7.224	$\frac{kg}{s}$
$Y_{ v r}$	-0.845	-1.113	$\frac{kg}{s}$
$Y_{ r r}$	-3.450	-3.481	$\frac{kg}{s}$
N_v	0.000	0.000	$\frac{kg}{s}$
$N_{ v v}$	-0.209	-0.0342	$\frac{kg}{s}$
$N_{ r v}$	0.08	0.158	$\frac{kg}{s}$
N_r	-6.916	-6.905	$\frac{kg}{s}$
$N_{ r r}$	-4.734	-4.825	$\frac{kg}{s}$
N_{rrr}	-0.147	-0.068	$\frac{kg}{s}$
$N_{ v r}$	0.08	0.075	$\frac{kg}{s}$

Table 3.1: Grey-box model parameter values and estimated parameter values.

3.1.3 Discussion

By comparing the original parameter values to the estimated values in Table 3.1 it can be seen that the system identification method is able to find the underlying model structure with added noise. The parameters are not identical due to the added noise but lie very close to the original ones. These results also indicates that the experiments presented in Appendix A are sufficient regarding to collect enough information about the system to be able to identify the model parameters.

3.2 milliAmpere

milliAmpere is an autonomous experimental platform with the purpose of testing and developing autonomous systems. The ferry has a rectangular shaped symmetric hull design. The propulsion system consists of two azimuth thrusters located at the centerline fore and aft of the vessel, 1.8m from CO. The vessel is fully electric and has a battery bank of 14.4kWh. The specification for the milliAmpere ferry can be found in Table 3.2.

Throughout the semester one week was intended to be used to perform experiments on the milliAmpere ferry. The experiments took place at the harbor basin near "Brattørkaia" in Trondheim. The ferry was launched on the 07.04.2019 after having rewiring and maintenance work

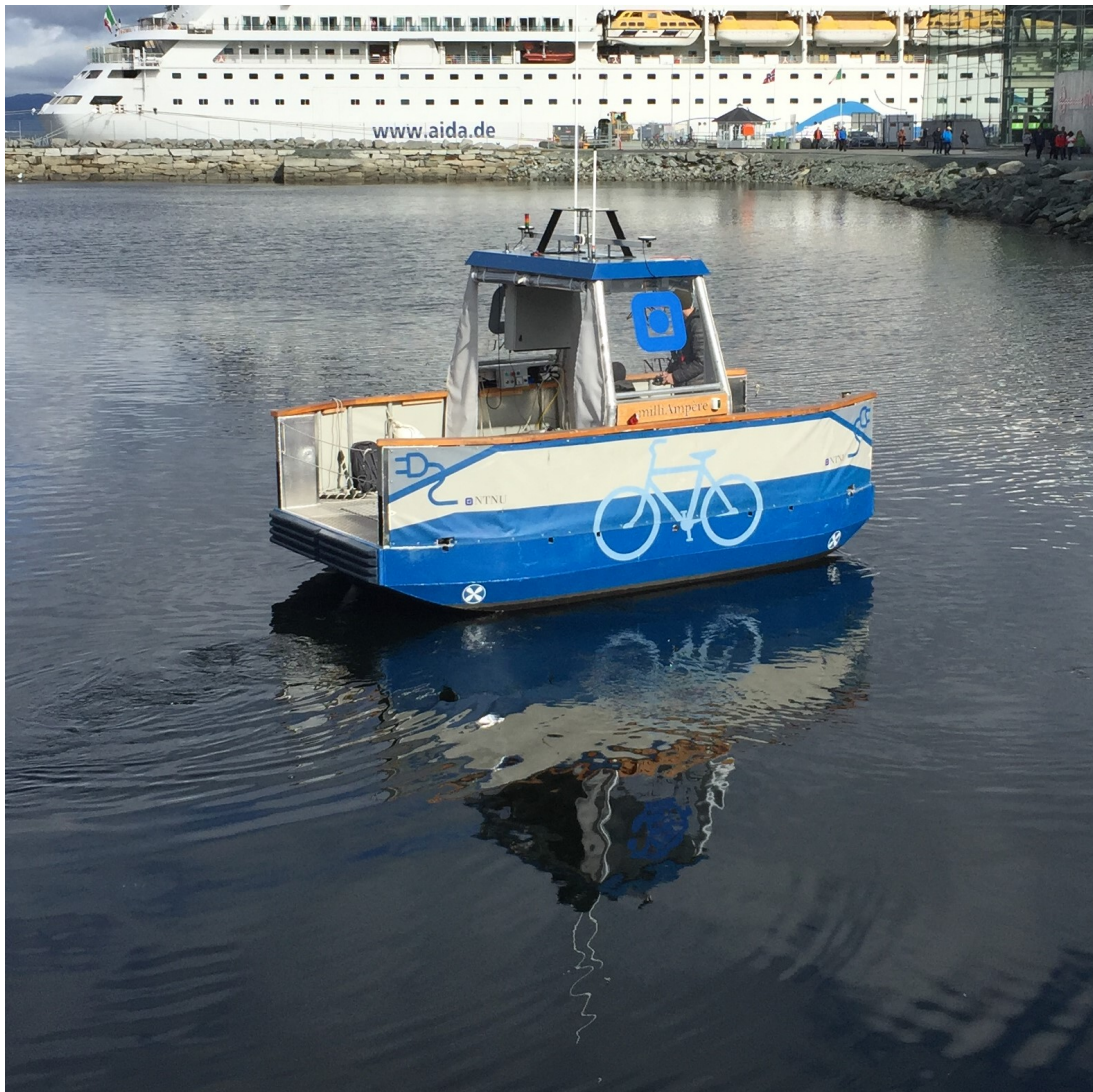


Figure 3.3: Me, Emil Thyri and Brage Sæther out performing experiments on the milliAmpere ferry at the harbor basin Brattørkaia on the 30.05.2019. Courtesy of Brage Sæther.

Component	Description
Hull length	5m
Hull Width	2.8m
Propulsion	2 × 2kW Azimuth Thrusters
Battery	6 × 2.4kWh
Positioning	VECTOR VS330, GNSS and RTK
Sensors	Xsens MTi-10 IMU, Radar, Lidar

Table 3.2: milliAmpere spesifications.

during the winter. As the experiments were very dependent on having good weather conditions, several test days were postponed. In May it was an incident including the milliAmpere ferry which led to usage prohibition. The experiments on the ferry had to be further postponed, and the experiments took place in week 22. The final data was gathered on the 30.05.2019.

When performing the experiments the control system aboard was used. The control system gives out a value between $[-100, 100]\%$. By using a mapping between percent, rpm and thrust force, the input value coming from the control system is converted to thrust. This mapping is necessary to be able to convert rpm measurements to newton in the system identification method. The mapping is found in Appendix D is developed by using the results of a bollard pull test found in Appendix C. Figure 3.4 shows the relationship between rpm and Newton. During the execution of the motion experiments presented in Appendix A there was experienced difficulties. As the experiments are performed outside, there are specially two external factors that will influence the system significantly, that is wind and ocean-currents. At the test day the wind-speed was about $1 - 3 \frac{m}{s}$ with wind-gusts up to $6 \frac{m}{s}$ classified as light breeze according to the Beaufort Scale (for Maritime Meteorology, 1970). It was experienced that even small wind-speeds influenced the ferry motion, and this caused some challenges with the non-coupled motion tests making them drift into coupled motion. This resulted in that the non-coupled motion tests were done by manual control of the ferry with the remote radio-control to compensate for external forces. The effect of this will be discussed in section 3.5.

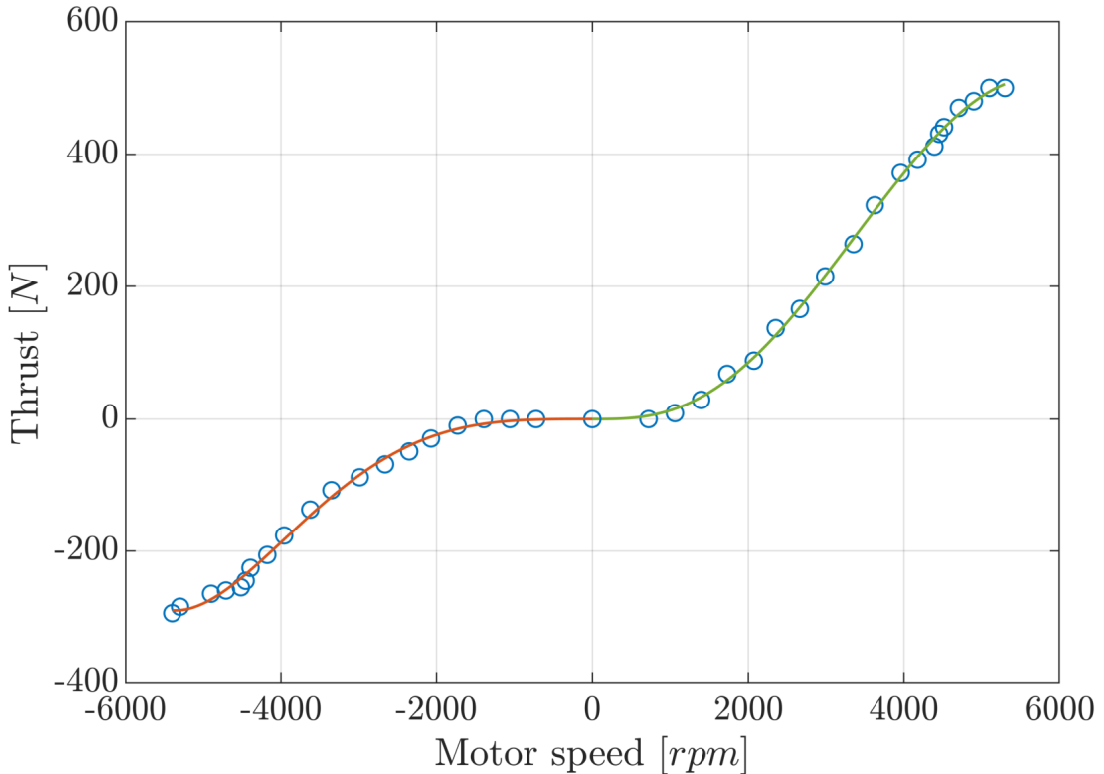


Figure 3.4: Mapping between rpm and Newton for one thruster, by using tables in Appendix D.

3.3 Surge-Decoupled Model for milliAmpere

By using the surge-decoupled model structure presented in Section 3.1 a solution is found by solving the NLP.

3.3.1 Problem Formulation

The problem formulation for the surge-decoupled model is the same as in (3.5) through (3.7), with the weights presented in Table 3.3. The model parameters to be identified are:

$$\begin{aligned} \mathbf{P} = [m_{11}, m_{22}, m_{23}, m_{32}, m_{33}, X_u, X_{|u|u}, X_{uuu}, \\ Y_v, Y_{|v|v}, Y_{vvv}, Y_{|r|v}, Y_r, Y_{|v|r}, Y_{|r|r}, N_v, N_{|v|v}, N_{|r|v}, N_r, N_{|r|r}, N_{rrr}, N_{|v|r}] \quad (3.9) \end{aligned}$$

Weight	Value
λ	0.001
\mathbf{W}_{surge}	diag(1, 0.1, 0.1)
\mathbf{W}_{sway}	diag(0.1, 1, 0.1)
\mathbf{W}_{yaw}	diag(0.1, 0.1, 1)
\mathbf{W}_{all}	diag(1, 1, 1)

Table 3.3: Weighting parameters for the surge-decoupled model.

The value for the hyperparameter was found by trying out several values and used the one that gave least error in the verification set. The weights are chosen such that it reduces the effect of coupled motion during the noncoupled tests in surge, sway and yaw. It is also added an inequality constraint for the linear terms in the damping matrix (2.15) to ensure it to be positive definite. The inequality constraint is

$$h(\mathbf{w}) = \begin{bmatrix} X_u \\ X_u(Y_v N_r - Y_r N_v) \end{bmatrix} > \mathbf{0} \quad (3.10)$$

3.3.2 Identification Results

The identification results with the surge-decoupled model (3.2)-(3.4) for the milliAmpere are presented in Figure 3.5, showing the estimated and measured velocities. The identified parameters are presented in Table 3.4. Figure 3.6 shows the measured input.

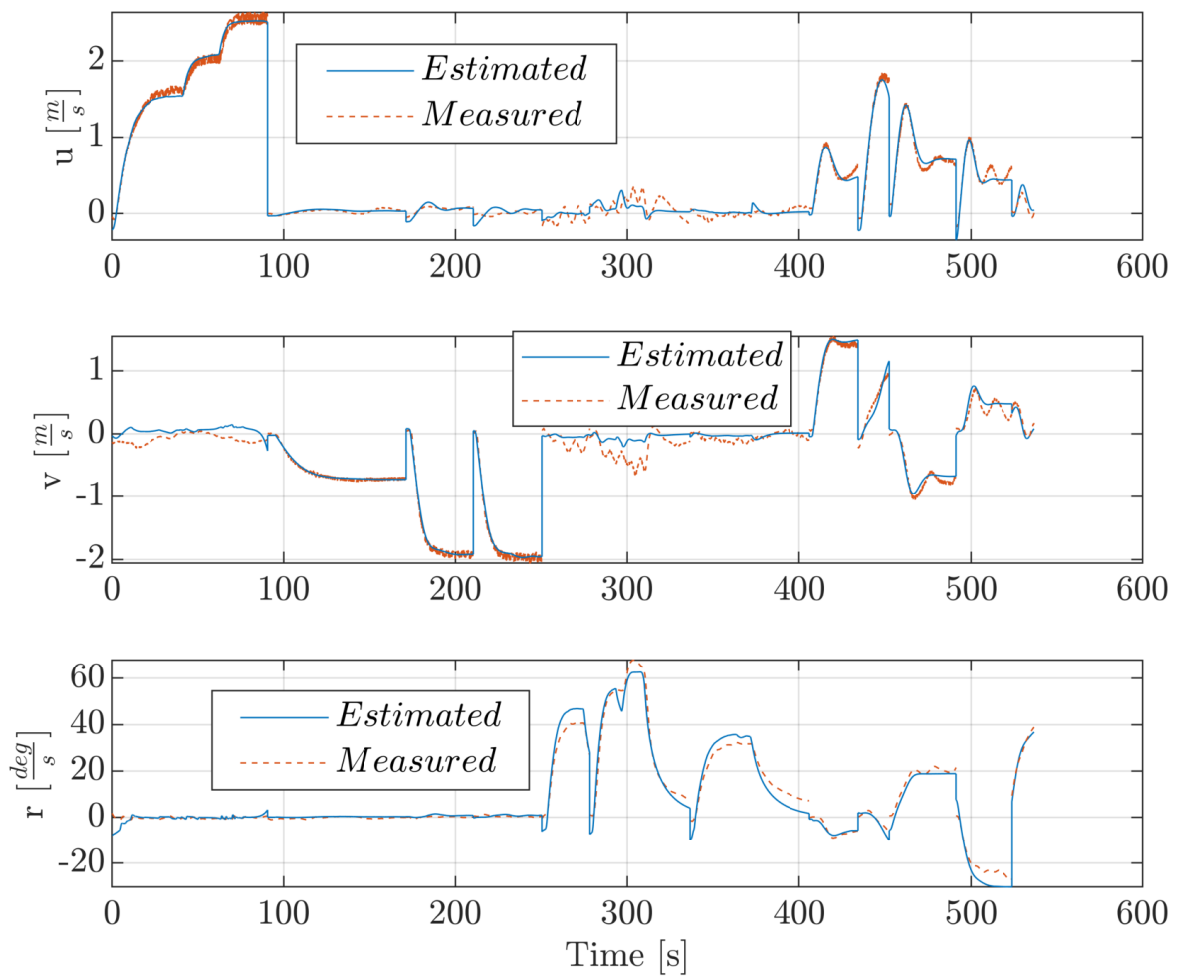


Figure 3.5: Experimental data and estimated velocities after the parameters have been identified for the surge-decoupled model.

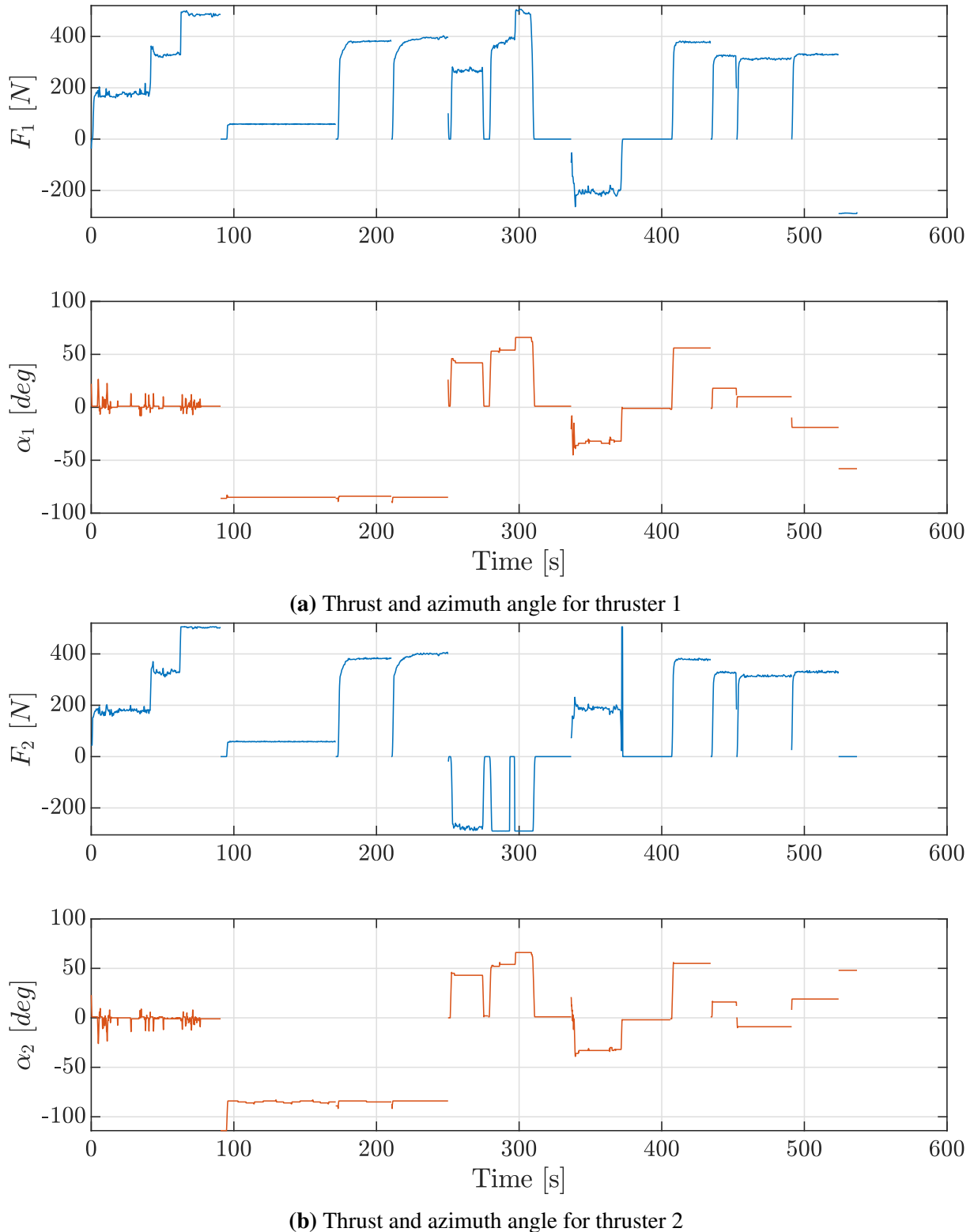


Figure 3.6: Experimental data used in the parameter estimation for the surge-decoupled model. Thrust and azimuth angle for the two thrusters on the milliAmpere ferry.

Parameter	Estimated Value	Unit
m_{11}	2389.657	kg
m_{22}	2533.911	kg
m_{23}	62.386	kg
m_{32}	28.141	kg
m_{33}	5068.910	kgm^2
X_u	-27.632	$\frac{kg}{s}$
$X_{ u u}$	-110.064	$\frac{kg}{s}$
X_{uuu}	-13.965	$\frac{kg}{s}$
Y_v	-52.947	$\frac{kg}{s}$
$Y_{ v v}$	-116.486	$\frac{kg}{s}$
Y_{vvv}	-24.313	$\frac{kg}{s}$
$Y_{ r v}$	-1540.383	$\frac{kg}{s}$
Y_r	24.732	$\frac{kg}{s}$
$Y_{ v r}$	572.141	$\frac{kg}{s}$
$Y_{ r r}$	-115.457	$\frac{kg}{s}$
N_v	3.524	$\frac{kg}{s}$
$N_{ v v}$	-0.832	$\frac{kg}{s}$
$N_{ r v}$	336.827	$\frac{kg}{s}$
N_r	-122.860	$\frac{kg}{s}$
$N_{ r r}$	-874.428	$\frac{kg}{s}$
N_{rrr}	0.000	$\frac{kg}{s}$
$N_{ v r}$	-121.957	$\frac{kg}{s}$

Table 3.4: Estimated parameter values for surge-decoupled model.

3.3.3 Verification

By using data from experiments that are not used in the identification process the surge-decoupled models performance is evaluated. The model is simulated with a RK4 method and compared with the experimental data. The verification results are presented in Figure 3.7. The error from the verification can be seen in Figure 3.8.

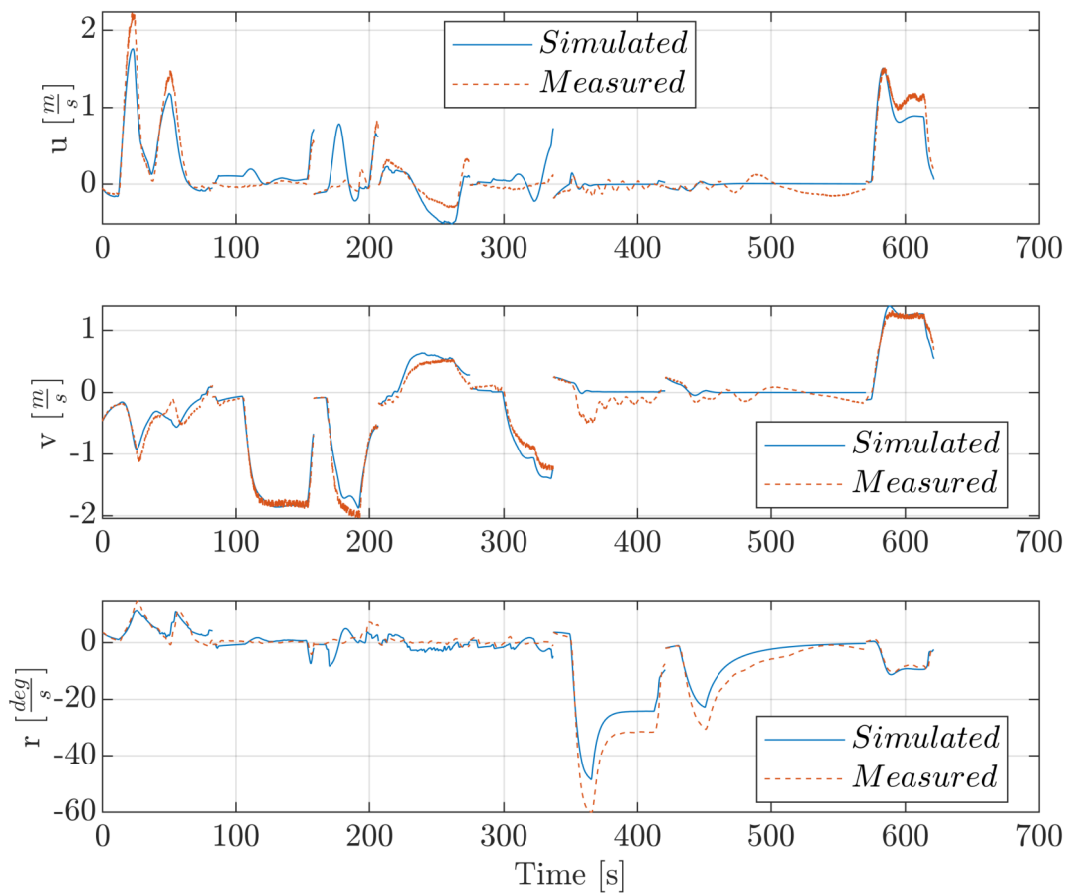


Figure 3.7: Comparison of experimental data and simulated data with the parameters for surge-decoupled model.

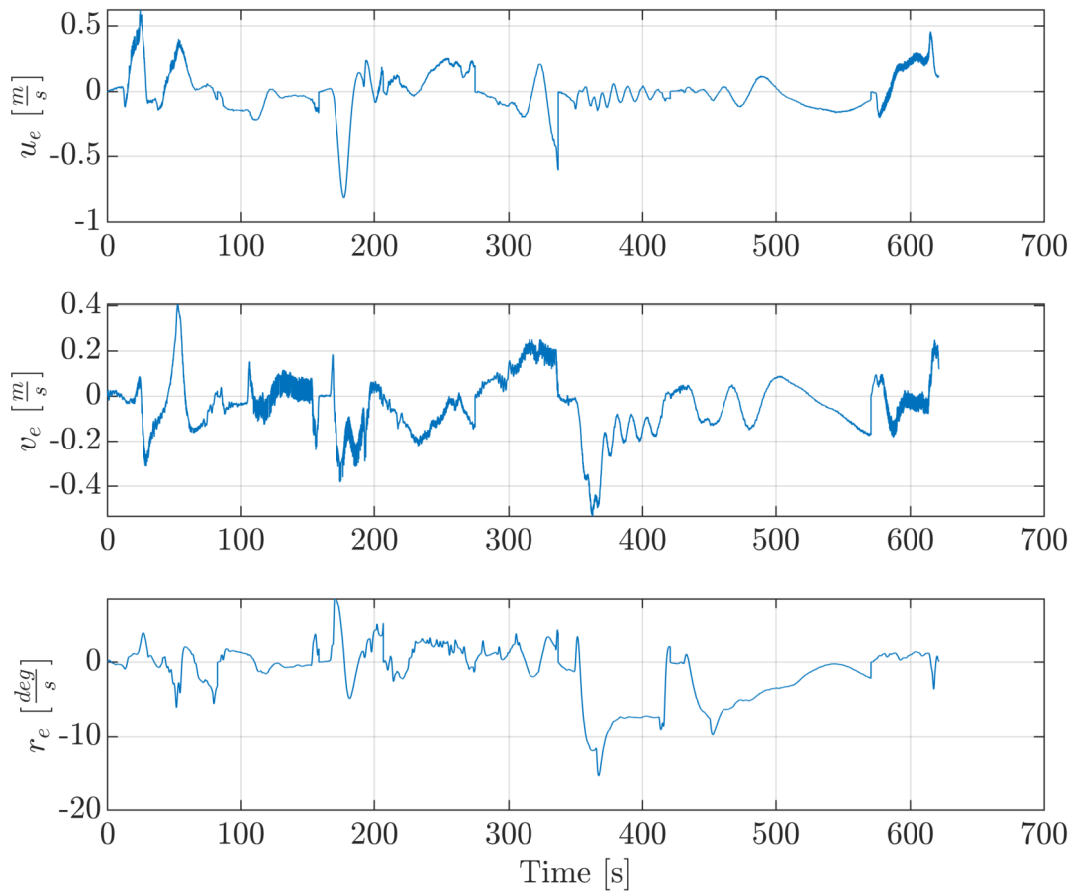


Figure 3.8: Showing the error between experimental and simulated data with the surge-decoupled model.

3.3.4 Discussion

The identification results show that the estimated velocities are fitting quite well to the measured. It can be seen in Figure 3.5 that the estimation of the noncoupled surge and sway velocities is performing well. has some deviation for the noncoupled steps in surge, sway and yaw. These effects may be a result of that CO is deviating from CG, as well as influence by external forces.

The verification results are confirming that the model is able to predict velocities reasonably well. It can be seen in Figures 3.7 and 3.8 that the model is under-predicting surge and yaw velocities but predicts sway with good accuracy.

3.4 Fully-Coupled Model for milliAmpere

By using the fully-coupled model structure, a solution is found by solving the NLP. A recap from chapter 2. The model is expressed as

$$\mathbf{M}\dot{\boldsymbol{\nu}} + \mathbf{C}(\boldsymbol{\nu})\boldsymbol{\nu} + \mathbf{D}(\boldsymbol{\nu})\boldsymbol{\nu} = \boldsymbol{\tau} \quad (3.11)$$

with \mathbf{M} , $\mathbf{C}(\boldsymbol{\nu})$ and $\mathbf{D}(\boldsymbol{\nu})$ defined by the fully coupled structure are given by

$$\mathbf{M} = \begin{bmatrix} m_{11} & m_{12} & m_{13} \\ m_{21} & m_{22} & m_{23} \\ m_{31} & m_{32} & m_{33} \end{bmatrix} \quad (3.12)$$

$$\mathbf{C}(\boldsymbol{\nu}) = \begin{bmatrix} 0 & 0 & c_{13}(\boldsymbol{\nu}) \\ 0 & 0 & c_{23}(\boldsymbol{\nu}) \\ c_{31}(\boldsymbol{\nu}) & c_{32}(\boldsymbol{\nu}) & 0 \end{bmatrix} \quad (3.13)$$

$$\mathbf{D}(\boldsymbol{\nu}) = \begin{bmatrix} d_{11}(\boldsymbol{\nu}) & d_{12} & d_{13} \\ d_{21} & d_{22}(\boldsymbol{\nu}) & d_{23}(\boldsymbol{\nu}) \\ d_{31} & d_{32}(\boldsymbol{\nu}) & d_{33}(\boldsymbol{\nu}) \end{bmatrix}. \quad (3.14)$$

3.4.1 Problem Formulation

The problem formulation for the fully coupled model is the same as in (3.5) through (3.7) with the fully-coupled structure given by (3.12) through (3.14). The weights are presented in Table 3.5. By using the same experimental data as in surge-decoupled model the parameters for the fully-coupled model are identified. The model parameters to be identified are:

$$\mathbf{P} = [m_{11}, m_{12}, m_{13}, m_{21}, m_{22}, m_{23}, m_{31}, m_{32}, m_{33}, X_u, X_{|u|u}, X_{uuu}, X_v, X_r, Y_u, Y_v, Y_{|v|v}, Y_{vvv}, Y_{|r|v}, Y_r, Y_{|v|r}, Y_{|r|r}, N_u, N_v, N_{|v|v}, N_{|r|v}, N_r, N_{|r|r}, N_{rrr}, N_{|v|r}] \quad (3.15)$$

Weight	Value
λ	0.001
\mathbf{W}_{surge}	diag(1, 0.1, 0.1)
\mathbf{W}_{sway}	diag(0.1, 1, 0.1)
\mathbf{W}_{yaw}	diag(0.1, 0.1, 1)
\mathbf{W}_{all}	diag(1, 1, 1)

Table 3.5: Weighting parameters for the fully coupled model.

The value for the hyperparameter is found by trying out several values and used the one that gave least error in the verification set. It is also added an inequality constraint for the linear terms in the damping matrix (2.15) to ensure it to be positive definite. The inequality constraint is

$$h(\mathbf{w}) = \begin{bmatrix} X_u \\ X_u(Y_v N_r - Y_r N_v) \end{bmatrix} > \mathbf{0} \quad (3.16)$$

3.4.2 Identification Results

The identification results for the fully coupled model for milliAmpere are presented in Figure 3.9, showing the estimated and measured velocities. The identified parameters are presented in Table 3.6 and Figure 3.6 shows the measured model input.

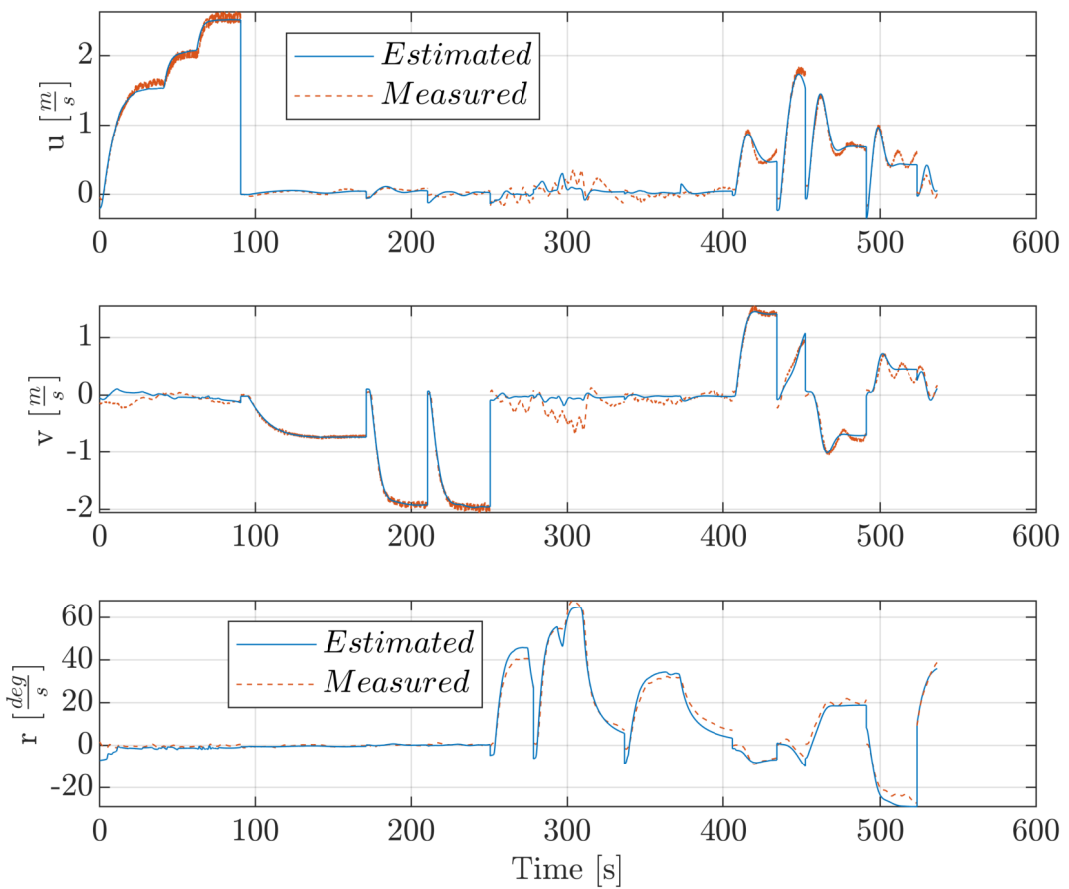


Figure 3.9: Experimental data and estimated velocities after the parameters has been identified for the fully coupled model.

Parameter	Estimated Value	Unit
m_{11}	2389.173	kg
m_{12}	-12.536	kg
m_{13}	39.776	kg
m_{21}	27.147	kg
m_{22}	2530.602	kg
m_{23}	-20.612	kg
m_{31}	112.965	kg
m_{32}	-0.606	kg
m_{33}	5068.800	kgm^2
X_u	-27.408	$\frac{kg}{s}$
$X_{ u u}$	-107.555	$\frac{s}{kg}$
X_{uuu}	-14.874	$\frac{kg}{s}$
X_v	39.398	$\frac{kg}{s}$
X_r	104.568	$\frac{kg}{s}$
Y_u	-45.037	$\frac{kg}{s}$
Y_v	-61.927	$\frac{kg}{s}$
$Y_{ v v}$	-84.895	$\frac{kg}{s}$
Y_{vvv}	-45.394	$\frac{s}{kg}$
$Y_{ r r}$	-1475.115	$\frac{kg}{s}$
Y_r	35.525	$\frac{kg}{s}$
$Y_{ v r}$	546.700	$\frac{kg}{s}$
$Y_{ r r}$	-60.848	$\frac{kg}{s}$
N_u	41.789	$\frac{s}{kg}$
N_v	16.464	$\frac{s}{kg}$
$N_{ v v}$	-18.003	$\frac{s}{kg}$
$N_{ r v}$	320.144	$\frac{s}{kg}$
N_r	-120.483	$\frac{s}{kg}$
$N_{ r r}$	-870.050	$\frac{s}{kg}$
N_{rrr}	0.000	$\frac{s}{kg}$
$N_{ v r}$	-271.946	$\frac{s}{kg}$

Table 3.6: Estimated parameter values for the fully coupled model.

3.4.3 Verification

By using data from experiments that are not used in the identification process the fully-coupled model's performance is evaluated. The model is simulated with a RK4 method and compared with the experimental data. The verification results are presented in Figure 3.10. The error from the verification can be seen in Figure 3.10.

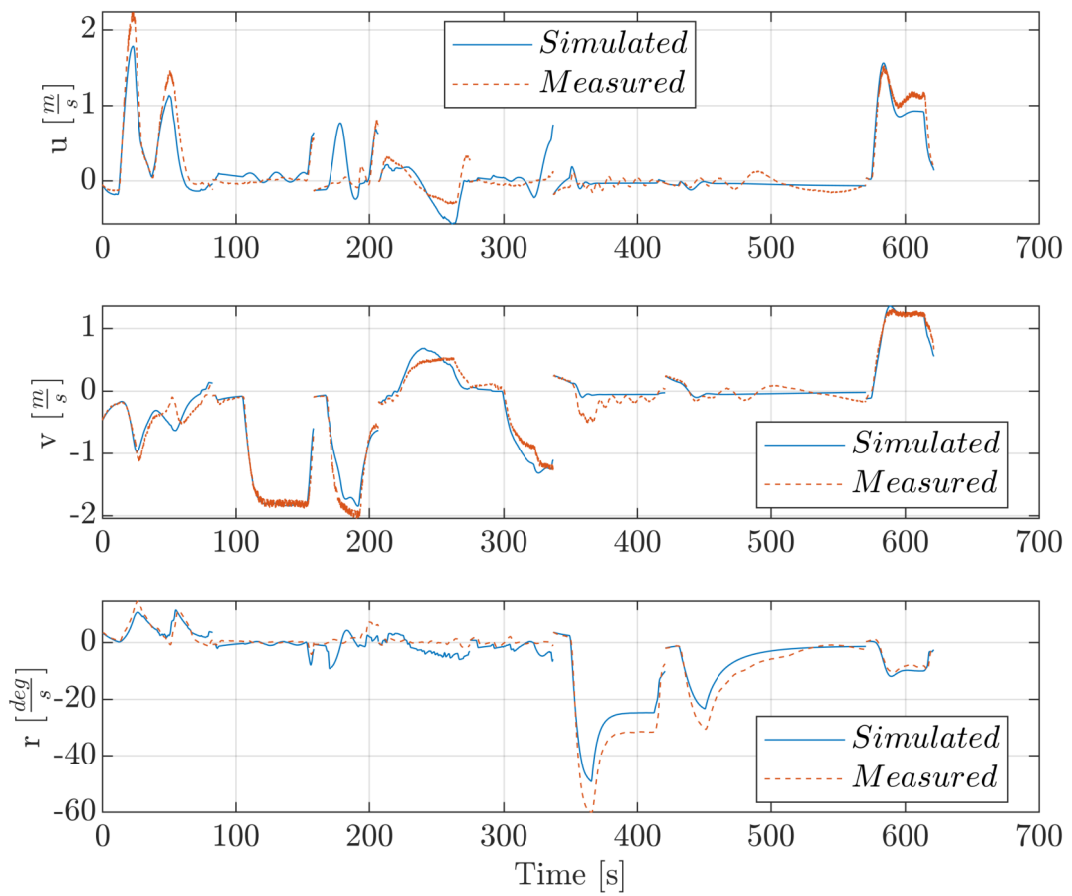


Figure 3.10: Comparison of experimental data and simulated values with the estimated parameters for fully coupled model.

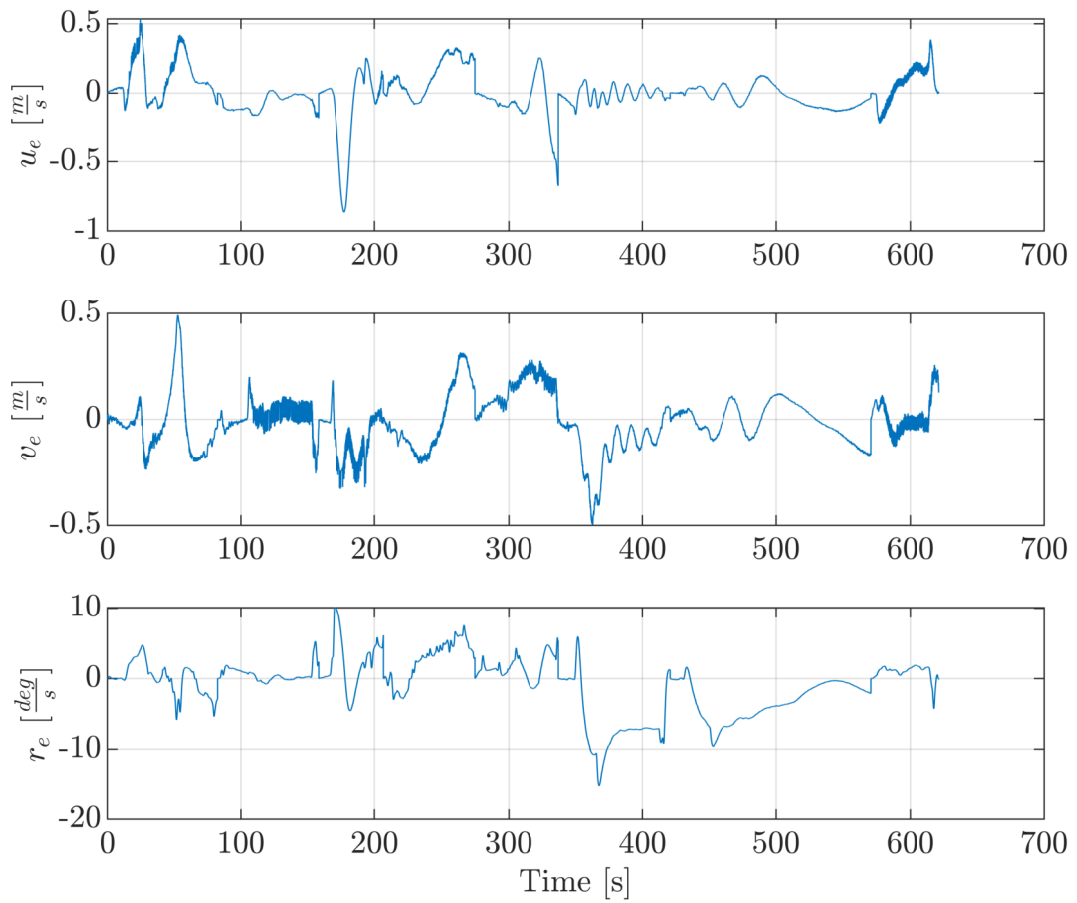


Figure 3.11: Showing the error between experimental data and simulated with the fully coupled model.

3.5 Summary & Discussion of the Ship Model Results

The identification results in Figure 3.5 and 3.9 shows that the fully-coupled model has similar results as the surge-decoupled model. The estimated velocities are following the measured well. Also, on the measured velocities there is an oscillating pattern in surge and sway during the steps in yaw. This are most likely coming from that CO deviates from CG. In the proposed models, it is assumed that CO equals CG and this is reflected in the results as the estimated surge and sway velocities seems to be close to zero during steps in yaw. This can also be seen in the verification results, in Figure 3.7 and 3.10, as the simulated surge and sway velocity is close to zero when rotating in yaw.

In Table 3.7 a comparison between the two models can be seen. The best values are presented as bold fonts. The fully-coupled model has less mean-absolute-error on predicting surge and yaw velocities but slightly more for the yaw velocity. Also, the fully-coupled model gives a lower objective function value.

In the verification of the two models it can be seen in Figure 3.7 and 3.10 that both models has some deviations at the transient peak in surge velocity, as if the model has more weight than it should. The same can be seen for the yaw velocity. In addition it seems like the yaw dynam-

	Surge-Decoupled Model	Fully-Coupled Model	Unit
$\frac{1}{N} \sum_{k=1}^N \bar{u}_k - u_k $	0.1062	0.1035	$\frac{m}{s}$
$\frac{1}{N} \sum_{k=1}^N \bar{v}_k - v_k $	0.0959	0.0966	$\frac{m}{s}$
$\frac{1}{N} \sum_{k=1}^N \bar{r}_k - r_k $	2.6468	2.7875	$\frac{deg}{s}$
$\phi(\mathbf{w}, \bar{\mathbf{w}})$	4.63545	4.53572	

Table 3.7: Mean absolute error between estimated and experimental data for velocities with surge-decoupled and fully coupled model. The bottom line shows the objective function value for the solution of the NLP.

ics has more damping than it should, as it has some stationary deviation around 400s. These deviations can also be a result of external forces acting on the vessel during the experiments.

The noncoupled tests were performed with manual control to compensate for external disturbances. In Figure 3.6 the compensation is clearly visible for the surge test. In the proposed models, external disturbances are not modelled. This does that the system identification method will try to compensate for the unknown external forces by adjusting the parameters so that the model will "generate" energy i.e a negative definite system, which is highly unwanted. This caused a challenge during the identification process as the estimated nonlinear damping matrix $D(\nu)$ turned out to not be positive definite. The linear damping terms are forced to build a positive definite linear damping matrix by the inequality constraint in (3.16). The same could not be done with the nonlinear damping terms as it turned out to be too demanding to calculate in the system identification method. However, as mentioned in section 2.4 the initial parameters guess is crucial to find a global optimal solution. As a result of this the diagonal model-elements was first identified. These elements were then locked with an allowed interval of $\pm 10\%$ of the identified parameter values. Then a new identification was run, identifying all of the model parameters using the results from the first identification as an initial parameter guess for the second. This gave a positive definite $D(\nu)$ for both the surge-decoupled model and the fully-coupled model.

Also there could be several other factors that can be a source of error in the identification of the ship models:

- Sensor uncertainty for the IMU .
- Sensor uncertainty for the GPS.
- CO deviates from CG.
- Influence of environmental forces like wind and currents.
- Variable mass distribution of the vessel due to people aboard the vessel during experiments.
- Interpolation in data processing.
- Delay caused by the embedded software and hardware.
- Cavitation of the propellers.
- Inaccuracy in the rpm to Newton mapping.

3.6 Azimuth Model for milliAmpere

Recap from Chapter 2, The candidate model for the azimuth angle dynamics is expressed as

$$\dot{\alpha} = K_\alpha \frac{(\alpha_d - \alpha)}{\sqrt{(\alpha_d - \alpha)^2 + \epsilon^2}}. \quad (3.17)$$

3.6.1 Problem Formulation

By using the NLP as defined in (2.40) with the azimuth angles $\boldsymbol{\alpha} = [\alpha_1, \alpha_2]$ and the desired angles $\boldsymbol{\alpha}_d = [\alpha_{d1}, \alpha_{d2}]$ as input , the problem formulation for the azimuth angle model becomes

$$\min_{\boldsymbol{w}} \phi(\boldsymbol{w}, \bar{\boldsymbol{w}}) \quad (3.18a)$$

$$s.t \quad \mathbf{g}(\boldsymbol{w}) = \mathbf{0} \quad (3.18b)$$

$$h(\boldsymbol{w}) \leq 0. \quad (3.18c)$$

$$\boldsymbol{w}_{lb} \leq \boldsymbol{w} \leq \boldsymbol{w}_{ub} \quad (3.18d)$$

$$\boldsymbol{w}(0) = \bar{\boldsymbol{w}}(0) \quad (3.18e)$$

where

$$\phi(\boldsymbol{w}, \bar{\boldsymbol{w}}) = \sum_{j=1}^J \sum_{n=1}^{N_j} (\boldsymbol{\alpha}_{jn} - \bar{\boldsymbol{\alpha}}_{jn})^T \mathbf{W}_j (\boldsymbol{\alpha}_{jn} - \bar{\boldsymbol{\alpha}}_{jn}) + \lambda \mathbf{R}(\mathbf{P}) \quad (3.19a)$$

$$\boldsymbol{w} = [\boldsymbol{\alpha}_{10}^T, \boldsymbol{\alpha}_{11}^T, \dots, \boldsymbol{\alpha}_{1N}^T, \boldsymbol{\alpha}_{20}^T, \boldsymbol{\alpha}_{21}^T, \dots, \boldsymbol{\alpha}_{JN_J}^T, P^T]^T \quad (3.19b)$$

$$\bar{\boldsymbol{w}} = [\bar{\boldsymbol{\alpha}}_{10}^T, \bar{\boldsymbol{\alpha}}_{11}^T, \dots, \bar{\boldsymbol{\alpha}}_{1N_1}^T, \bar{\boldsymbol{\alpha}}_{20}^T, \bar{\boldsymbol{\alpha}}_{21}^T, \dots, \bar{\boldsymbol{\alpha}}_{JN_J}^T]^T \quad (3.19c)$$

and the equality constraints

$$g(\boldsymbol{w}) = \begin{bmatrix} \mathbf{F}(\boldsymbol{\alpha}_{10}, \bar{\boldsymbol{\alpha}}_{d_{10}}) - \boldsymbol{\alpha}_{11} \\ \vdots \\ \mathbf{F}(\boldsymbol{\alpha}_{1N_1-1}, \bar{\boldsymbol{\alpha}}_{d_{1N_1-1}}) - \boldsymbol{\alpha}_{1N_1} \\ \mathbf{F}(\boldsymbol{\alpha}_{20}, \bar{\boldsymbol{\alpha}}_{d_{20}}) - \boldsymbol{\alpha}_{21} \\ \vdots \\ \mathbf{F}(\boldsymbol{\alpha}_{JN_J-1}, \bar{\boldsymbol{\alpha}}_{d_{JN_J-1}}) - \boldsymbol{\alpha}_{JN_J} \end{bmatrix} = \mathbf{0} \quad (3.20)$$

The model parameters to be identified are:

$$\mathbf{P} = [K_{\alpha_1}, K_{\alpha_2}, \epsilon_1, \epsilon_2] \quad (3.21)$$

The weights can be seen in Table 3.8. As the ratio between model parameters and data points are relatively large the challenge with overfitting is marginal. Therefore, the hyperparameter λ is set to zero. As for the weighting matrix, it is set to diagonal one.

Weight	Value
λ	0
\mathbf{W}	diag(1, 1,)

Table 3.8: Weighting parameters for the azimuth angle model.

3.6.2 Identification Results

The experimental data is provided by following the test plan in Appendix B. By the experimental data and (3.17) as a candidate model in the identification method, the parameters are identified. The identification results for the azimuth angle model are presented in Figure 3.12, showing the estimated, measured and reference azimuth angle. The identified parameters are presented in Table 3.9.

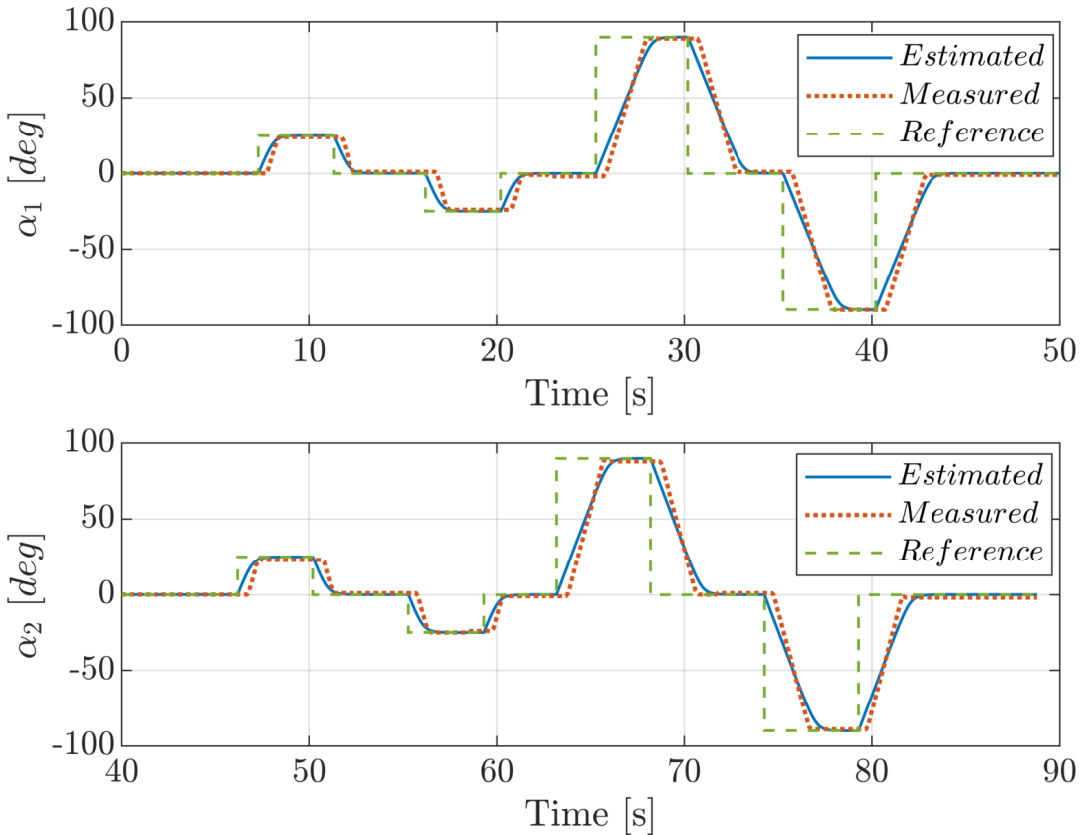


Figure 3.12: Experimental data and estimated azimuth angles after the parameters has been identified for the azimuth-angle model.

Parameters	Estimated value
K_{α_1}	34.458
K_{α_2}	37.526
ϵ_1	6.277
ϵ_2	7.721

Table 3.9: Parameters for Azimuth angle model

3.6.3 Verification

The verification results are presented in Figure 3.14. The error from the verification can be seen in Figure 3.15.

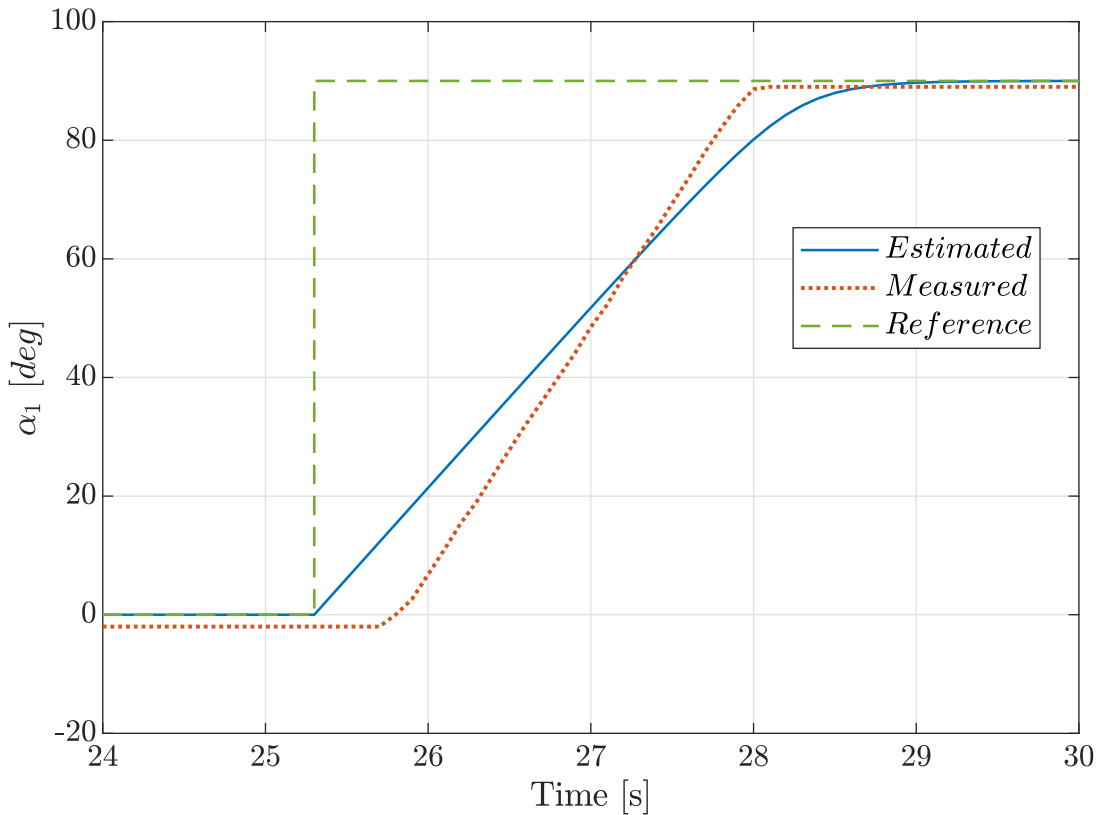


Figure 3.13: Delay in the azimuth dynamics.

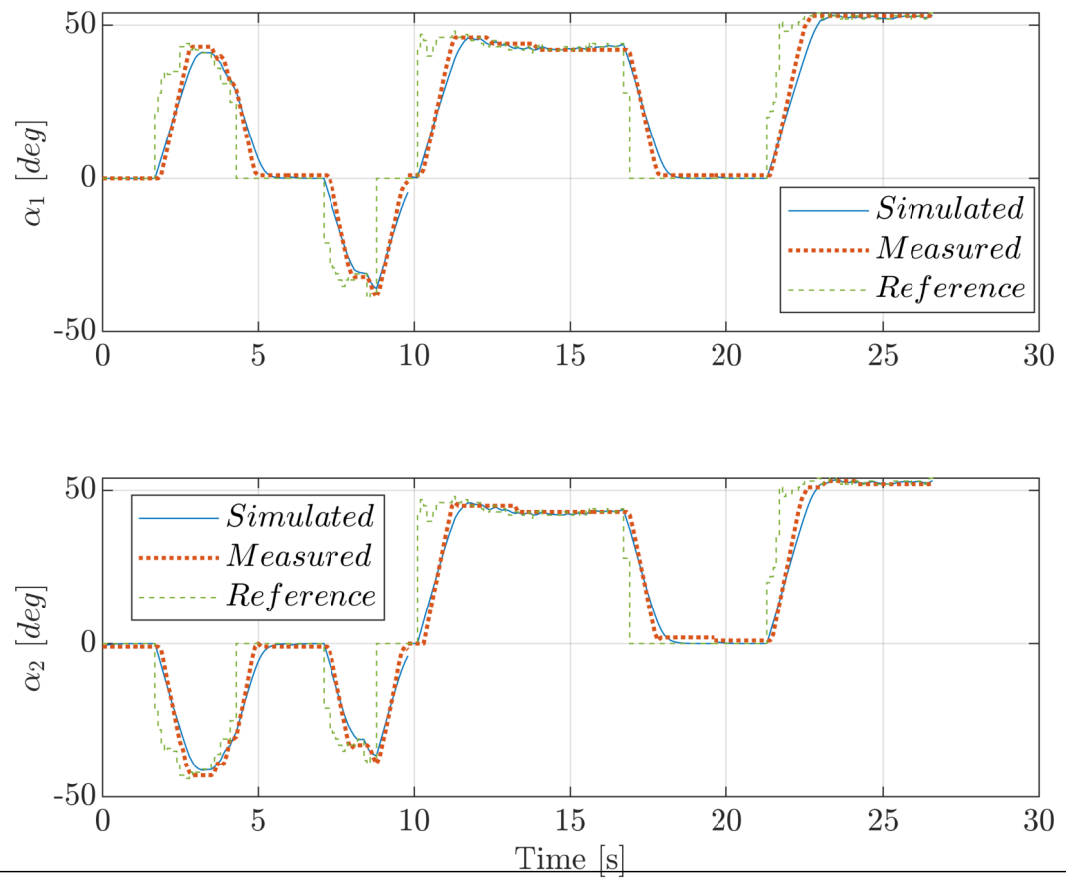


Figure 3.14: Comparison of experimental data and simulated values for Azimuth angle model.

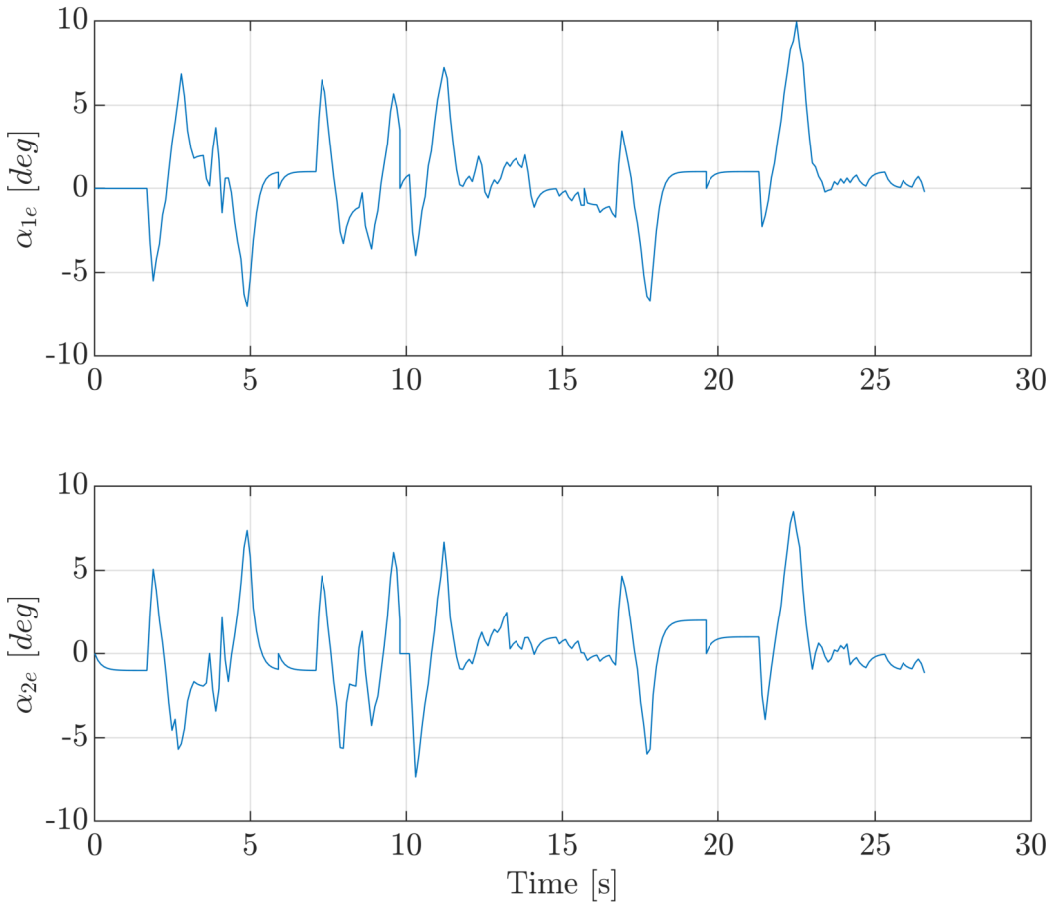


Figure 3.15: Error between experimental data and simulated azimuth angle.

3.6.4 Discussion

The identification results show that the estimated azimuth angle is fitting the measured well. However, it is a significant time delay in the azimuth dynamics. It takes about 0.4 seconds for the azimuth servo to respond to the reference input. This delay can be seen in Figure 3.13. Time delay is not modelled in the proposed azimuth model and it seems that this is the main source to the error shown in Figure 3.15. There could be several sources for this time delay:

- Sampling time for the controller loop
- Backlash in gear between azimuth servo and azimuth shaft.
- Backlash in azimuth shaft and encoder.
- Delay in electronic communication.
- Delay in reading and publishing encoder data.

The verification results show that the model is giving errors in the transient parts of the motion. The proposed model seems to fit the actual behaviour very well, but is under-performing due to time delay in the thruster-control system.

Also, during the analysis of the azimuth identification results a bug connected to the thruster-control system was discovered and fixed. When the azimuth servo was ordered to go clockwise after a step in reference angle, the immediate response was a short counter-clockwise motion before moving in the desired clockwise direction. This behaviour can be seen in Figure 2.4 in Chapter 2.

3.7 Motor-Speed Model for milliAmpere

A recap from Chapter 2. The motorspeed model is expressed as

$$\dot{\omega} = K_{\omega}(\omega_d - \omega), \quad (3.22)$$

3.7.1 Problem Formulation

By using the NLP as defined in (2.40) with the azimuth angles $\omega = [\omega_1, \omega_2]$ and the desired angles $\omega_d = [\omega_{d1}, \omega_{d2}]$ as input , the problem formulation for the azimuth angle model becomes

$$\min_{\mathbf{w}} \phi(\mathbf{w}, \bar{\mathbf{w}}) \quad (3.23a)$$

$$s.t \quad \mathbf{g}(\mathbf{w}) = \mathbf{0} \quad (3.23b)$$

$$h(\mathbf{w}) \leq 0. \quad (3.23c)$$

$$\mathbf{w}_{lb} \leq \mathbf{w} \leq \mathbf{w}_{ub} \quad (3.23d)$$

$$\mathbf{w}(0) = \bar{\mathbf{w}}(0) \quad (3.23e)$$

where

$$\phi(\mathbf{w}, \bar{\mathbf{w}}) = \sum_{j=1}^J \sum_{n=1}^{N_j} (\omega_{jn} - \bar{\omega}_{jn})^T \mathbf{W}_j (\omega_{jn} - \bar{\omega}_{jn}) + \lambda \mathbf{R}(\mathbf{P}) \quad (3.24a)$$

$$\mathbf{w} = [\omega_{10}^T, \omega_{11}^T, \dots, \omega_{1N_1}^T, \omega_{20}^T, \omega_{21}^T, \dots, \omega_{JN_J}^T, P^T]^T \quad (3.24b)$$

$$\bar{\mathbf{w}} = [\bar{\omega}_{10}^T, \bar{\omega}_{11}^T, \dots, \bar{\omega}_{1N_1}^T, \bar{\omega}_{20}^T, \bar{\omega}_{21}^T, \dots, \bar{\omega}_{JN_J}^T]^T \quad (3.24c)$$

and the equality constraints

$$g(\mathbf{w}) = \begin{bmatrix} \mathbf{F}(\omega_{10}, \bar{\omega}_{d10}) - \omega_{11} \\ \dots \\ \mathbf{F}(\omega_{1N_1-1}, \bar{\omega}_{d1N_1-1}) - \omega_{1N_1} \\ \mathbf{F}(\omega_{20}, \bar{\omega}_{d20}) - \omega_{21} \\ \dots \\ \mathbf{F}(\omega_{JN_J-1}, \bar{\omega}_{dJN_J-1}) - \omega_{JN_J} \end{bmatrix} = \mathbf{0} \quad (3.25)$$

The model parameters to be identified are:

$$\mathbf{P} = [K_{\omega_1}, K_{\omega_2}] \quad (3.26)$$

The weights can be seen in Table 3.10. As the ratio between model parameters and data points are relatively large the challenge with overfitting is marginal. Therefore, the hyperparameter λ is set to zero. As for the weighting matrix, it is set to diagonal one.

Weight	Value
λ	0
\mathbf{W}	diag(1, 1)

Table 3.10: Weighting parameters for the motorspeed model

3.7.2 Identification Results

The experimental data is provided by following the test plan in Appendix B. By using the experimental data and (3.22) as a candidate model in the identification method, the parameters are identified. The current version of CasADI (v.3.4.5) has a challenge with handling large values for the decision variables. The experimental data of motor speed has the unit rpm which has a relatively large magnitude. This implies that for the identification of motor-speed dynamics the data had to be scaled down before being used in the identification method. After the identification the data was re-scaled back to the original quantity. This is simply implemented by using a scaling constant. The identification results for the motor-speed model are presented in Figure 3.16, showing the estimated, measured and reference motor speed. The identified parameters are presented in Table 3.11.

Parameters	Estimated value
K_{ω_1}	0.563
K_{ω_2}	0.591

Table 3.11: Parameters for motor speed model

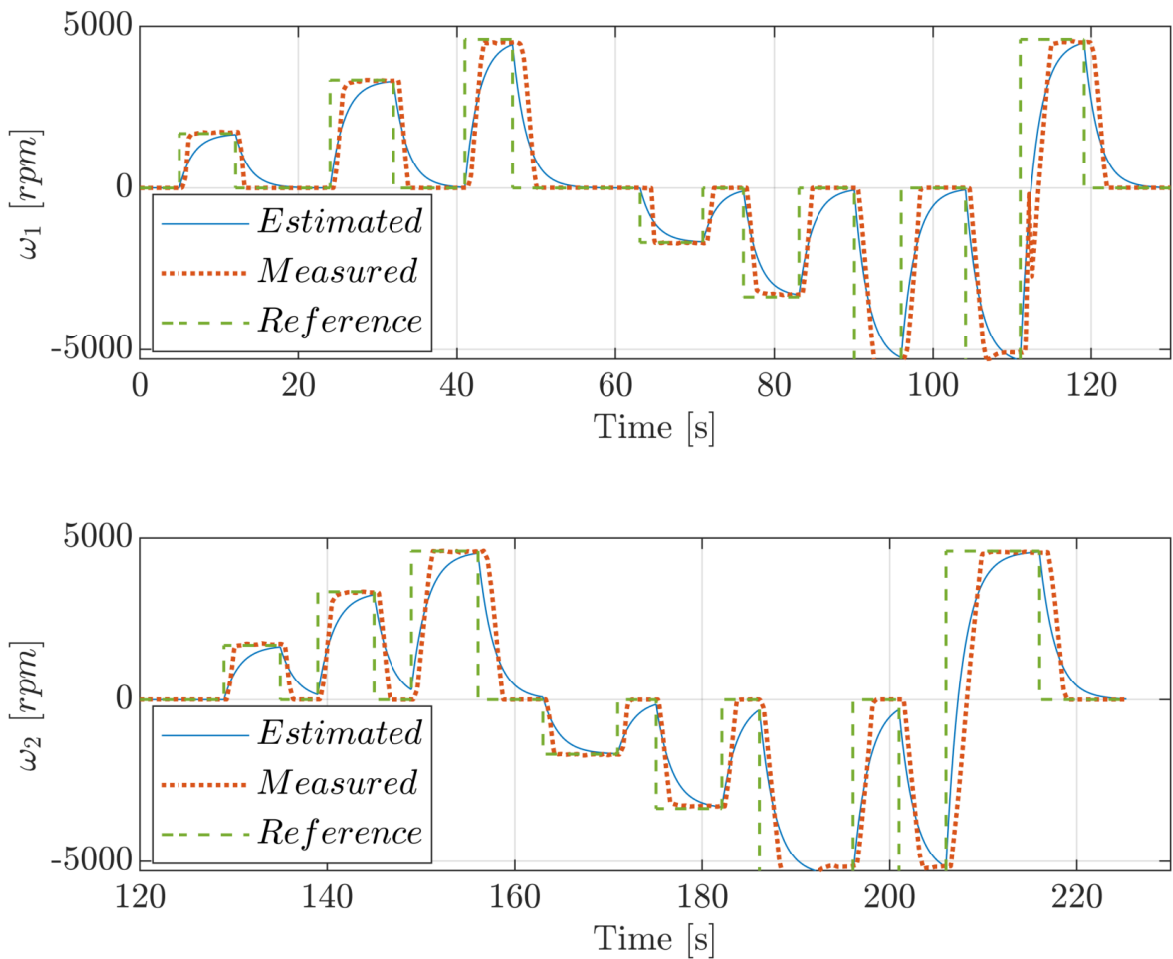


Figure 3.16: Experimental data and estimated motor speeds after the parameters has been identified for the motor-speed model.

3.7.3 Verification

The verification results are presented in Figure 3.17 showing the comparison between simulated and measured motor speed. The error from the verification can be seen in Figure 3.18.

3.7.4 Discussion

The identification results show that the estimated motor-speeds fits the measurements with some deviations, specially in the transient part. Although it is difficult to get information about the underlying model dynamics of the motor speeds due to the large sampling time of 0.42 seconds, the first order model seem to give a decent prediction. The verification results seems to show better performance, as the simulated motor speeds follows the measured with reasonable good accuracy, as seen in Figure 3.17. An explanation could be that the reference data in the identification part is a step, while the reference-data in the verification part is coming from the remote controller. This will give a smoother reference trajectory which is easier for the model

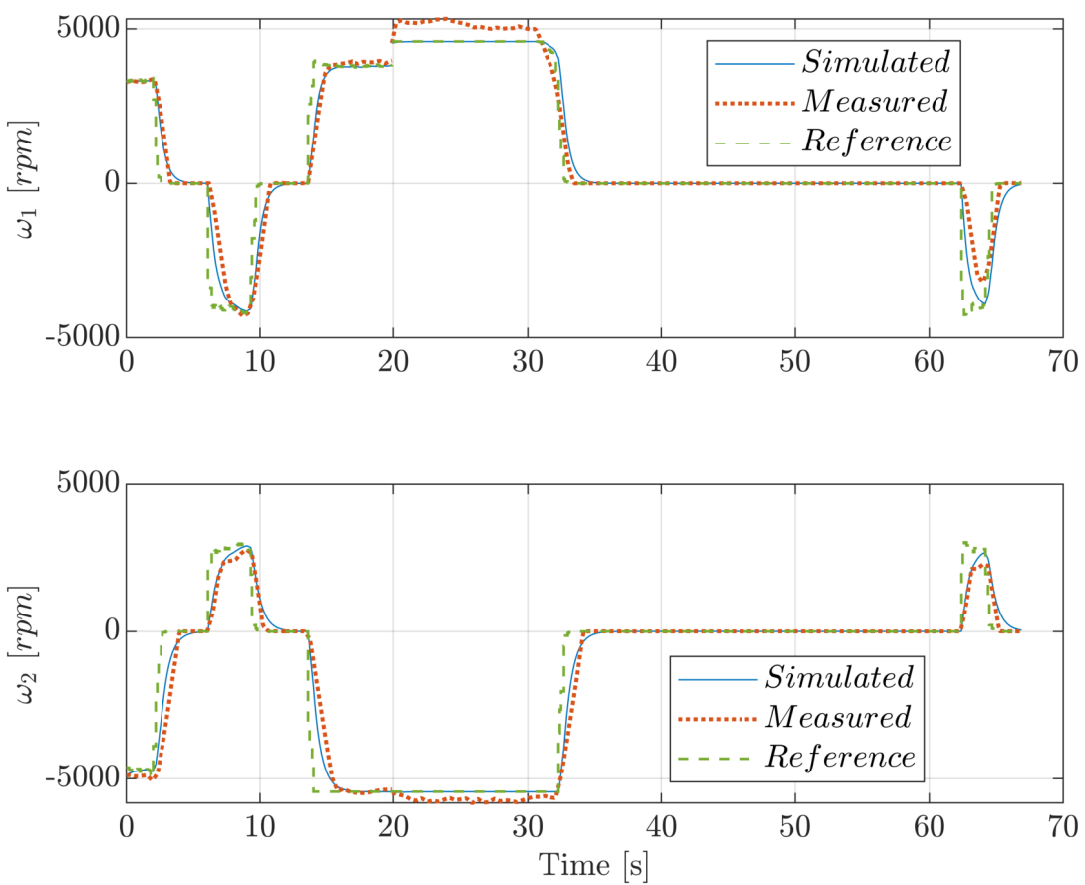


Figure 3.17: Comparison of experimental data and simulated values for motor-speed model.

to follow.

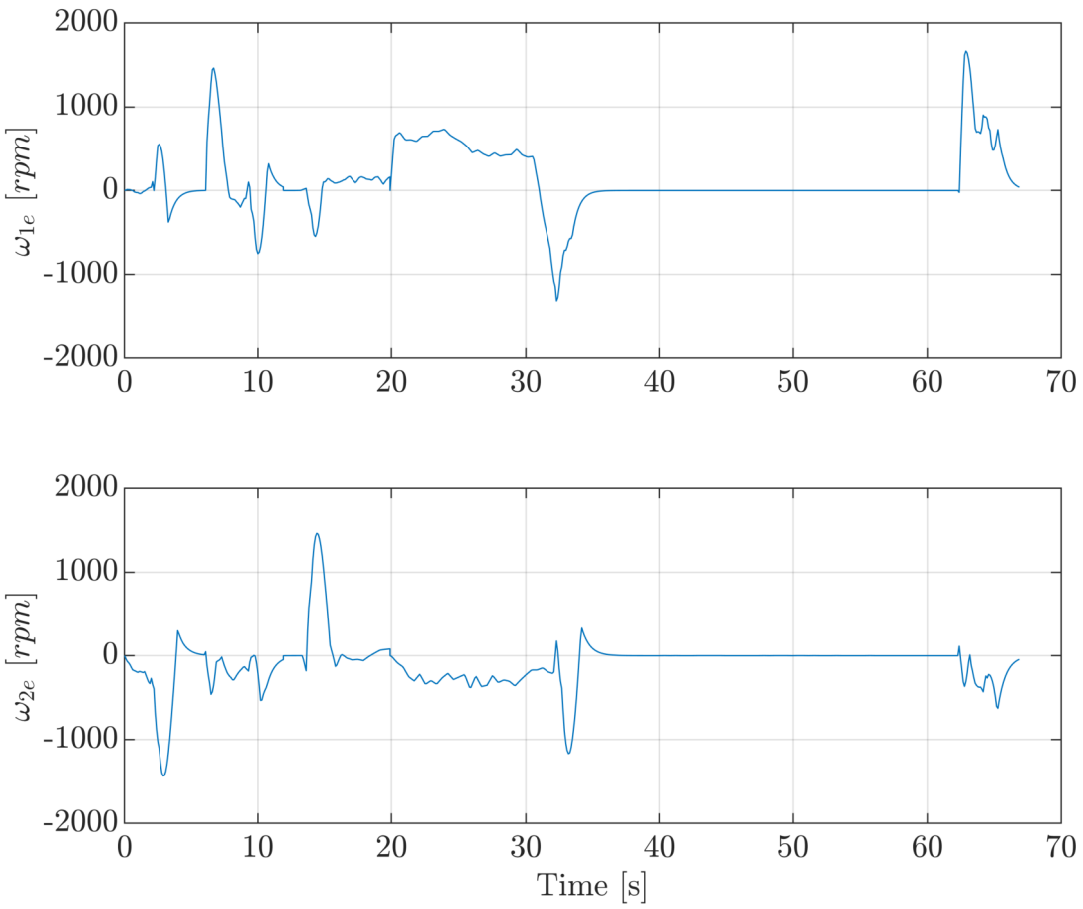


Figure 3.18: Error between experimental data and simulated motor speed.

3.8 Applications of the Models

The presented models in this thesis are suitable for many applications like simulation, prototyping, motion control, collision avoidance etc. The models have already been used to develop motion control and collision avoidance systems. By using (2.2) a feed-forward controller can be expressed as:

$$\boldsymbol{\tau}_{FF} = \mathbf{M}\dot{\boldsymbol{\nu}}_d + \mathbf{C}(\boldsymbol{\nu}_d) + \mathbf{D}(\boldsymbol{\nu}_d). \quad (3.27)$$

where the desired acceleration and velocities are coming from a reference filter. The reference filter is generating a feasible smooth trajectory. More about how the models are used for navigation and motion control can be found in (Sæther, 2019).

In (Thyri, 2019) the surge-decoupled model is used to develop collision avoidance systems. In Figure 3.19 it can be seen a collision avoidance scenario where the surge-decoupled model is used to simulate the behaviour of the ferry.

Today as the computing power is at a relative high level, it makes it possible to have a digital twin. A digital twin is in this context a digital replica of a vessel described using mathematics. The idea is to have a dynamic ship model that runs in real time together with the physical vessel. This can be used for control and decision taking, fault detection and diagnosis, real-time optimization, predict errors before they happen, update dynamic models when they deviate

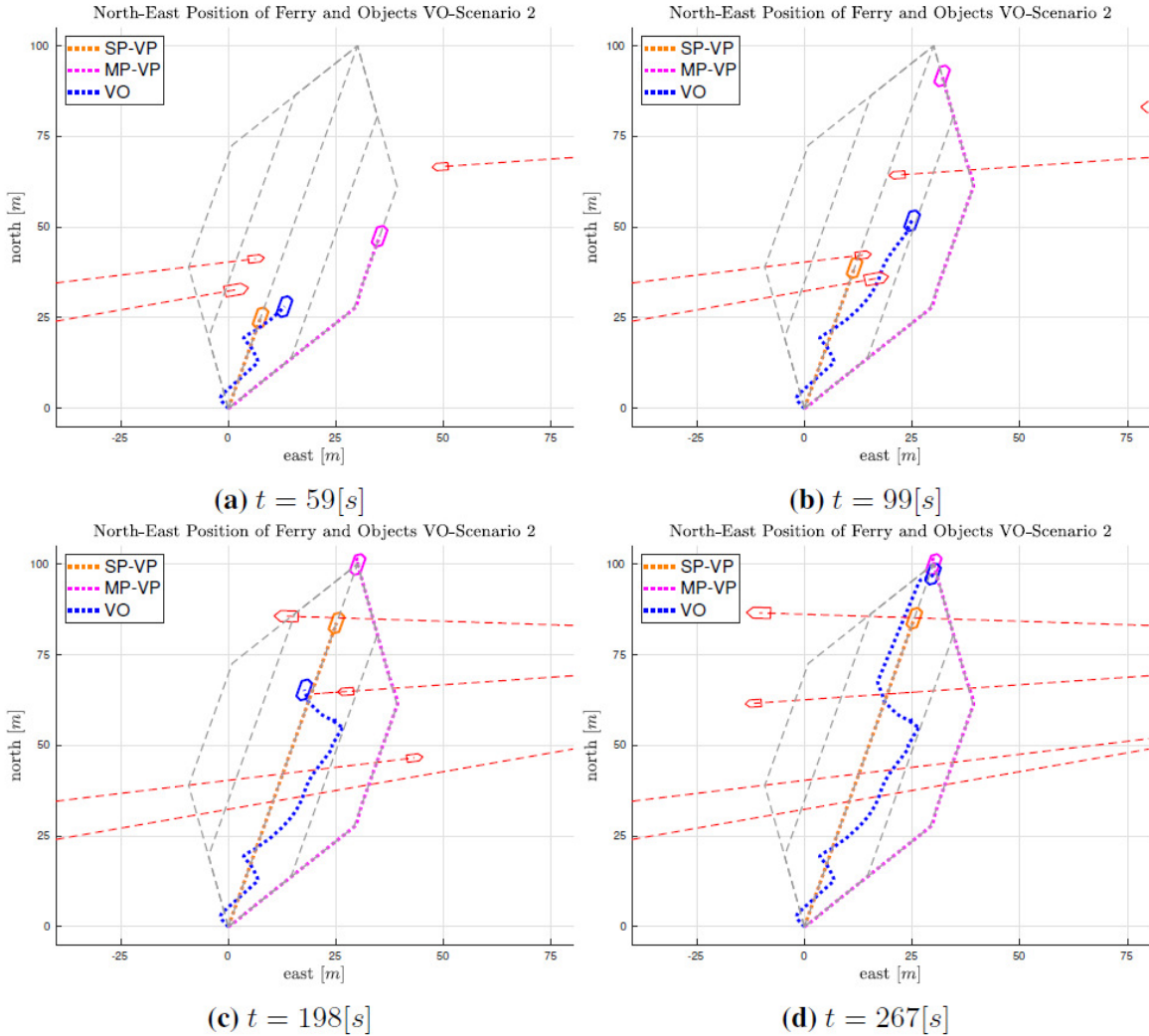


Figure 3.19: Collision avoidance scenarios. Blue, purple and orange are avoiding the red objects by using different collision-avoidance methods. Courtesy of Thyri (2019).

from the real dynamics of the vessel etc. The identified models in this thesis can be used in the foundation for a digital twin for the milliAmpere ferry.

Chapter 4

Conclusion & Further Work

Throughout this thesis, an optimization based identification method has been implemented, verified and used to identify the dynamics of the milliAmpere ferry and its propulsion system. The identified models are:

- A 3DOF Fully-coupled ship model.
- A 3DOF Surge-decoupled ship model.
- Azimuth angle model.
- Motorspeed model.
- Wind-load model.

By designing and performing experiments, experimental data is obtained and used in the identification method. The method is based on optimal control theory and by solving an NLP, an optimal solution is found that gives the estimated model parameters. By reproducing the parameters of a grey-box model with good accuracy the method is verified. The surge-decoupled parameters can be found in Table 3.4 and the fully-coupled model parameters can be found in Table 3.6. The dynamics of milliAmpere ferry is well described by the two identified ship models. Both of the models are performing well and give similar results. The fully coupled model has a marginally better performance but it is advantageous to use the surge-decoupled model as it is a less complex model. The thruster dynamics is well explained by the proposed azimuth and motor-speed model. Both can be used together with the proposed ship models to form a simulator of the milliAmpere ferry. The thruster model parameters can be found in Table 3.9 and Table 3.11. In addition to the ship and thruster dynamics, a wind model based on the ship's projected area is proposed. The proposed wind model correspond well with the experienced wind influence on the vessel during experiments.

The following further work can be considered:

- Improve the system identification methods abilities to handle process and measurement noise to avoid parameter drift due to external disturbances and sensor inaccuracy.
- Design a speed controller to be used for gathering experimental data.
- The presented models gives a foundation for the concept of a digital twin. Further research on what is required towards a full implementation of a digital twin.

- Automatic system identification.

Bibliography

- Andersson, J. A. E., Gillis, J., Horn, G., Rawlings, J. B., Diehl, M., 2018. CasADi – A software framework for nonlinear optimization and optimal control. Mathematical Programming Computation.
- Bitar, G., 2018. Report on performing system identification using simulation as a predictor, unpublished report, Norwegian University of Science and Technology, Trondheim, Norway.
- Bitar, G. I., 2017. Towards the development of autonomous ferries. Master's thesis, Norwegian University of Science and Technology, Trondheim, Norway.
- Eriksen, B.-O. H., Breivik, M., 2017. Modeling, identification and control of high-speed ASVs: Theory and experiments. In: Sensing and Control for Autonomous Vehicles. Springer International Publishing, pp. 407–431.
URL https://doi.org/10.1007/978-3-319-55372-6_19
- for Maritime Meteorology, W. M. O. C., 1970. The Beaufort Scale of Wind Force: (technical and Operational Aspects). Reports on marine science affairs. WMO.
- Fossen, T. I., apr 2011. Handbook of Marine Craft Hydrodynamics and Motion Control. John Wiley & Sons, Ltd.
URL <https://doi.org/10.1002/9781119994138>
- Fossen, T. I., Sagatun, S. I., Sørensen, A. J., Mars 1996. Identification of dynamically positioned ships. Control Engineering Practice 4 (3), 369–376.
URL [https://doi.org/10.1016/0967-0661\(96\)00014-7](https://doi.org/10.1016/0967-0661(96)00014-7)
- Gros, S., October 2017. Numerical optimal control, lecture 4: Shooting methods.
- Hastie, Trevor. Tibshirani, R. F. J., 2009. The Elements of Statistical Learning. Springer.
- Heggdal, K., Jun 2016. Trondheim kan bli først i verden på førerløse passasjerferjer. Adressa.
URL <https://www.adressa.no/nyheter/trondheim/2016/06/09/trondheim-kan-bli-frst-i-verden-p-frerlse-passasjerferjer-12862564.ece>
- Lyngstadaas, O. N., Sæterdal, T. E., Sørensen, M. E. N., Breivik, M., aug 2018. Improvement of ship motion control using a magnitude-rate saturation model. In: 2018 IEEE Conference on Control Technology and Applications (CCTA). IEEE, Copenhagen, Denmark.
URL <https://doi.org/10.1109/ccta.2018.8511451>

Nocedal, J., Wright, S. J., 2006. Numerical Optimization. Springer New York.

URL <https://doi.org/10.1007/978-0-387-40065-5>

Pedersen, A. A., December 2018. System identification with experiments for the milliampere ferry, specialization Project, Unpublished report. Department of Engineering Cybernetics, Norwegian University of Science and Technology, Trondheim, Norway.

Pivano, L., April 2008. Thrust estimation and control of marine propellers in four- quadrant operations. Ph.D. thesis, Norwegian University of Science and Technology, Trondheim, Norway.

Rolls-Royce, 2018. Rolls-Royce and Finferries demonstrate worlds first fully autonomous ferry. Press release www.rolls-royce.com.

URL <https://www.rolls-royce.com/media/press-releases/2018/03-12-2018-rr-and-finferries-demonstrate-worlds-first-fully-autonomous.aspx>

Sæther, B., 2019. Development and testing of navigation and motion control systems for milliampere. Master's thesis, Norwegian University of Science and Technology, Trondheim, Norway.

Skredderberget, A., Mar 2018. The first ever zero emission, autonomous ship. www.yara.com.

URL <https://www.yara.com/knowledge-grows/game-changer-for-the-environment/>

SNAME, 1950. Nomenclature for Treating the Motion of a Submerged Body Through a Fluid. Technical and research bulletin. The Society of Naval Architects and Marine Engineers.

URL <https://books.google.no/books?id=VqNFGwAACAAJ>

Stensvold, T., Sep 2018. Her demonstrerer de selvkjørende milliampere - nå skal de bygge ferge på 12 meter. Teknisk Ukeblad.

URL <https://www.tu.no/artikler/her-demonstrerer-de-selvkjorende-milliampere-pa-12-meter>

Taylor, M. E., 06 2000. System identification and control of an Arleigh Burke class destroyer using an extended Kalman filter. Master's thesis, University of South Carolina.

Thyri, E. H., 2019. A path-velocity decomposition approach to collision avoidance for autonomous passenger ferries. Master's thesis, Norwegian University of Science and Technology, Trondheim, Norway.

Torben, T. R., Brodkorb, A. H., Sørensen, A. J., 2019. Control allocation for double-ended ferries with full-scale experimental results. In: Submitted to 2019 Conference on Control Applications in Marine Systems (CAMS). KAIST, Daejeon, South Korea.

Wächter, A., Biegler, L. T., apr 2005. On the implementation of an interior-point filter line-search algorithm for large-scale nonlinear programming. Mathematical Programming 106 (1), 25–57.

URL <https://doi.org/10.1007/s10107-004-0559-y>

Appendices

Appendix **A**

Test Plan for Coupled Tests

Model Identification Experiments on milliAmpere Test Plan for Motion Tests

Anders Aglen Pedersen

April 2019

Safety

When operating the vessel at sea it must always be two persons on board. The location of the safety equipment and a plan for act due to unsuspected events like loss of propulsion, system failure, power loss, fire etc. must be undergone for all operators.

Test goal

The main goal for this experiment is to gather transient and steady state data for coupled and uncoupled motion to be used in model identification of coupled ship model.

1 Test platform

The control system on board will be used for logging the desired input force and output velocities. The vessel has two thrusters than can rotate 360 degrees, $[-180^\circ, 180^\circ]$ where 0° is in surge. The control system will be used to manually set the desired input force. The system runs ROS which has implemented a tool called rosbag that is an unified console tool for recording data, playback data, and other operations. This will be used for logging data. Also during the experiments it is important to make the weight distribution of the vessel as balanced as possible. The persons aboard must be in positions such that the added mass wont affect center of gravity.

2 Identification experiment

This experiment consists of both uncoupled and coupled motion tests. The uncoupled tests will specially be used to achieve robust data for the diagonal inertia and damping terms in the model, while the coupled tests will generate data for the coupling terms in the model. The input force can be mapped in

$$\mathcal{T} = \{\tau \in \mathbb{R}^3 | -100\% \leq \tau \leq 100\%\},$$

where τ is the input force in percent. By using the control allocation, the azimuth angles and motor speeds are calculated by the control allocation when giving it the desired input force.

2.1 Uncoupled Motion Tests

Three tests in surge sway and yaw where the input force are incremented for each step. Make sure that a new rosbag is created and logging is started. Write down the time from the system clock.

Surge

$$\boldsymbol{\tau}_u \in \left\{ \begin{bmatrix} 40\% \\ 0 \\ 0 \end{bmatrix}, \begin{bmatrix} 60\% \\ 0 \\ 0 \end{bmatrix}, \begin{bmatrix} 80\% \\ 0 \\ 0 \end{bmatrix} \right\}, \quad (1)$$

1. Start at $\boldsymbol{\nu} = \mathbf{0}$, input force $\boldsymbol{\tau} = [0, 0, 0]^T$ and azimuth angles $\boldsymbol{\alpha} = [0, 0]^T$.
2. Start the step series according to (1) and let the vessel reach steady state for 5 seconds.
3. Set input force to zero and let the vessel come to full stop.
4. Initiate next command in (1) and let vessel reach steady state for 5 seconds.
5. Repeat 3 and 4 until last step in (1) is reached.

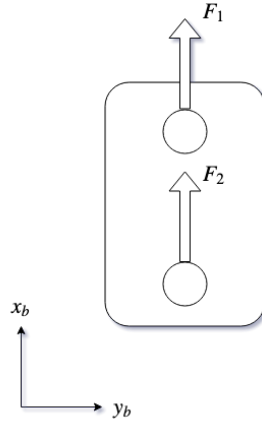


Figure 1: Surge test

Sway

$$\boldsymbol{\tau}_u \in \left\{ \begin{bmatrix} 0 \\ 40\% \\ 0 \end{bmatrix}, \begin{bmatrix} 0 \\ 60\% \\ 0 \end{bmatrix}, \begin{bmatrix} 0 \\ 80\% \\ 0 \end{bmatrix} \right\}, \quad (2)$$

1. Start at $\boldsymbol{\nu} = \mathbf{0}$, input force $\boldsymbol{\tau} = [0, 0, 0]^T$ and azimuth angles $\boldsymbol{\alpha} = [90^\circ, 90^\circ]^T$.
2. Start the step series according to (2) and let the vessel reach steady state for 5 seconds.
3. Set input force to zero and let the vessel come to full stop.
4. Initiate next command in (2) and let vessel reach steady state for 5 seconds.
5. Repeat 3 and 4 until last step in (2) is reached.

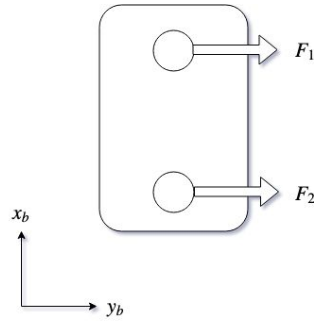


Figure 2: Surge test

Yaw

$$\tau_u \in \left\{ \begin{bmatrix} 0 \\ 0 \\ 40\% \end{bmatrix}, \begin{bmatrix} 0 \\ 0 \\ 60\% \end{bmatrix}, \begin{bmatrix} 0 \\ 0 \\ 80\% \end{bmatrix} \right\}, \quad (3)$$

1. Start at $\nu = \mathbf{0}$, input force $\tau = [0, 0, 0]^T$ and azimuth angles $\alpha = [90^\circ, -90^\circ]^T$.
2. Start the step series according to (3) and let the vessel reach steady state for 5 seconds.
3. Set input force to zero and let the vessel come to full stop.
4. Initiate next command in(3) and let vessel reach steady state for 5 seconds.
5. Repeat 3 and 4 until last step in (3) is reached.

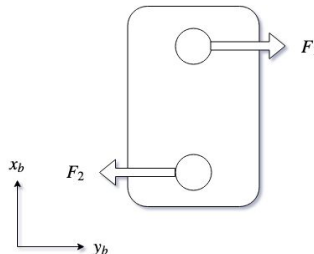


Figure 3: Surge test

2.2 Coupled Motion Tests

Two tests in surge-sway, surge-yaw and sway-yaw.

Surge-Sway

$$\tau_u \in \left\{ \begin{bmatrix} 40\% \\ 80\% \\ 0 \end{bmatrix}, \begin{bmatrix} 80\% \\ 40\% \\ 0 \end{bmatrix} \right\}, \quad (4)$$

1. Start at $\nu = 0$.
2. Start the step series according to (4) and let the vessel reach steady state for 5 seconds.
3. Set input force to zero and let the vessel come to full stop.
4. Initiate next command in (4) and let vessel reach steady state for 5 seconds.
5. Repeat 3 and 4 until last step in (4) is reached.

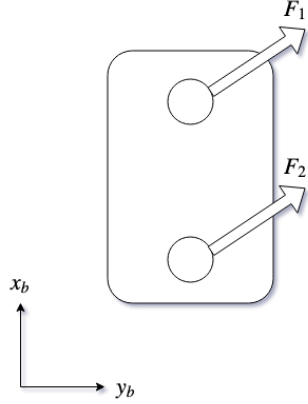


Figure 4: Surge test

Surge-Yaw

$$\tau_u \in \left\{ \begin{bmatrix} 40\% \\ 0 \\ 80\% \end{bmatrix}, \begin{bmatrix} 80\% \\ 0 \\ 40\% \end{bmatrix} \right\}, \quad (5)$$

1. Start at $\nu = 0$.
2. Start the step series according to (5) and let the vessel reach steady state for 5 seconds.
3. Set input force to zero and let the vessel come to full stop.
4. Initiate next command in (5) and let vessel reach steady state for 5 seconds.
5. Repeat 3 and 4 until last step in (5) is reached.

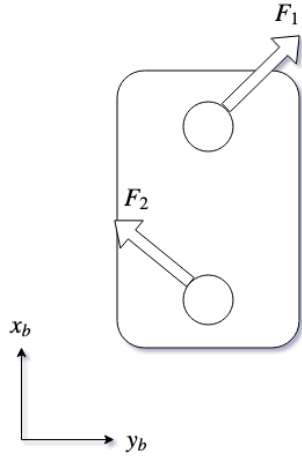


Figure 5: Surge test

Sway-Yaw

$$\tau_u \in \left\{ \begin{bmatrix} 0 \\ 40\% \\ 80\% \end{bmatrix}, \begin{bmatrix} 0 \\ 80\% \\ 40\% \end{bmatrix} \right\}, \quad (6)$$

1. Start at $\nu = 0$.
2. Start the step series according to (6) and let the vessel reach steady state for 5 seconds.
3. Set input force to zero and let the vessel come to full stop.
4. Initiate next command in (6) and let vessel reach steady state for 5 seconds.
5. Repeat 3 and 4 until last step in (6) is reached.

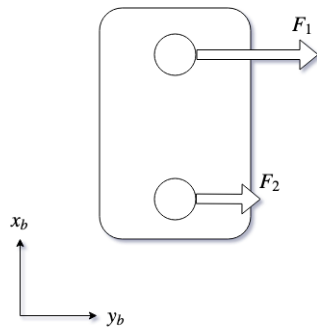


Figure 6: Surge test

Appendix **B**

Test Plan for Thrusters

Model Identification Experiments on milliAmpere Test Plan for Thrusters

Anders Aglen Pedersen

May 2019

Safety

When operating the vessel at sea it must always be two persons on board. The location of the safety equipment and a plan for act due to unsuspected events like loss of propulsion, system failure, power loss, fire etc. must be undergone for all operators.

Test goal

The main goal for this experiment is to gather transient and steady state data for thruster states, that is rotational velocity for the two propellers $[\omega_1, \omega_2]^T$ and azimuth angles $[\alpha_1, \alpha_2]^T$.

1 Test platform

The control system on board runs ROS which has implemented a tool called rosbag that is an unified console tool for recording data, playback data, and other operations. This will be used for logging data. The data consists of desired motor speeds and azimuth angles and the actual motor speed and azimuth angles. The vessel has two thrusters than can rotate ± 180 degrees, $[-180^\circ, 180^\circ]$ where 0° is in surge direction. The azimuth angle is given in degrees and motorspeed in percent of revolutions per minute [rpm]. The control system will be used to manually control the desired thruster force and angles.

2 Thruster Identification Experiment

The actuator space can be mapped in

$$\mathcal{A} = \{\boldsymbol{\alpha} \in \mathbb{S}^2 \mid -180^\circ \leq \alpha \leq 180^\circ\}$$

and

$$\mathcal{W} = \{\boldsymbol{\omega} \in \mathbb{R}^2 \mid -100\% \leq \omega \leq 100\%\}$$

where $\boldsymbol{\omega}$ is motorspeed in percent and $\boldsymbol{\alpha}$ is azimuth angle in degrees.

2.1 Experiment

Make sure that a new rosbag is created and logging is started. Write down the time from the system clock.

2.1.1 Azimuth angle test

Commanded steps for azimuth angles are given by

$$\boldsymbol{\alpha} \in \{(25, 25), (-25, -25), (90, 90), (-90, -90)\}^\circ$$

1. Start at $\boldsymbol{\alpha} = [0, 0]^T$ for azimuth angles.
2. Initiate first command in $\boldsymbol{\alpha}$ and let the thrusters reach desired azimuth angles.
3. Set azimuth angles to $\boldsymbol{\alpha} = [0, 0]^T$ and let the thrusters reach desired azimuth angles.
4. Initiate next command in $\boldsymbol{\alpha}$ and let the thrusters reach desired azimuth angles.
5. Repeat 3 and 4 until last step in $\boldsymbol{\alpha}$ is reached.

2.1.2 Motor speed test 1

This test maps the motorspeed dynamics from zero speed to a commanded speed then back to zero. The commanded steps for motorspeeds are given by

$$\boldsymbol{\omega} \in \{(25, 25), (50, 50), (100, 100), (-25, -25), (-50, -50), (-100, -100)\}\% \quad (1)$$

1. Start at $\boldsymbol{\nu} = 0$ and use $\boldsymbol{\alpha} = [90, 90]^T$ for thruster angles.
2. Start the step serie according to (1) and let the propellers reach steady state motion for 5 seconds
3. Set thrust force to zero and let the propellers come to full stop.
4. Initiate next command in (1) and let the propellers reach steady state motion for 5 seconds.
5. Repeat 3 and 4 until last step in (1) is reached.

2.1.3 Motor speed test 2

This test maps the motorspeed dynamics from a commanded step to another commanded step. The commanded steps for motorspeeds are given by

$$\boldsymbol{\omega} \in \{(-100, -100), (100, 100)\}\% \quad (2)$$

1. Start at $\boldsymbol{\nu} = 0$ and use $\boldsymbol{\alpha} = [90, 90]^T$ for thruster angles.
2. Start the step serie according to (2) and let the propellers reach steady state motion for 5 seconds
3. Initiate next command in (2) and let the propellers reach steady state motion for 5 seconds.
4. Set thrust force to zero and let the propellers come to full stop.

Appendix C

Bollard Pull Test

Bollard Pull Test

This test was performed by Tobias Torben, 06.06.2018.

Motor Speed [%]	FT 1[N]	FT 2[N]	FT Reversed [N]	RT [N]	Both Thrusters [N]
5	-	0	0	0	-
10	-	29.43	0	0	0
15	-	58.86	0	9.81	-
20	-	68.67	0	29.43	78.48
25	-	88.29	9.81	68.67	-
30	107.91	117.72	29.43	88.29	166.77
35	-	147.15	49.05	137.34	-
40	166.77	186.39	68.67	166.77	304.1
45	-	215.82	88.29	215.82	-
50	264.87	264.87	107.91	264.87	480.69
55	-	323.73	137.34	323.73	-
60	372.78	382.59	176.58	372.78	716.13
65	-	412.02	206.01	392.4	-
70	421.83	431.64	225.63	412.02	784.8
75	-	451.26	245.25	431.64	-
80	441.45	461.07	255.06	451.26	863.28
85	-	480.69	-	470.88	-
90	480.69	490.5	264.87	490.5	-
95	-	500.31	284.49	500.31	-
100	490.5	500.31	294.3	500.31	-

Table 1: Results from bollard pull test. FT: Front Thruster, RT: Rear Thruster.

Appendix **D**

Motor Speed to Thrust

Motor speed and Thrust

Anders Aglen Pedersen

Table showing a mapping between percent, forward/reversed motor-speed and thrust for the milliAmpere ferry. The reversed rpm is slightly higher than forward rpm at [90-100]% due to cavitation of the propellers.

[%]	Forward [rpm]	Thrust [N]	Reversed [rpm]	Reversed Thrust [N]
5	0	0	0	0
10	719	0	719	0
15	1056	9	1056	0
20	1392	29	1392	0
25	1728	68	1728	9
30	2071	88	2071	29
35	2351	137	2351	49
40	2662	166	2662	68
45	2987	215	2987	88
50	3352	264	3352	107
55	3625	323	3625	137
60	3960	372	3960	176
65	4177	392	4177	206
70	4393	412	4393	225
75	4455	431	4455	245
80	4517	441	4517	255
85	4708	470	4708	259
90	4900	480	4900	264
95	5100	500	5300	284
100	5300	500	5400	294

Table 1: Percent, rpm and thrust mapping.

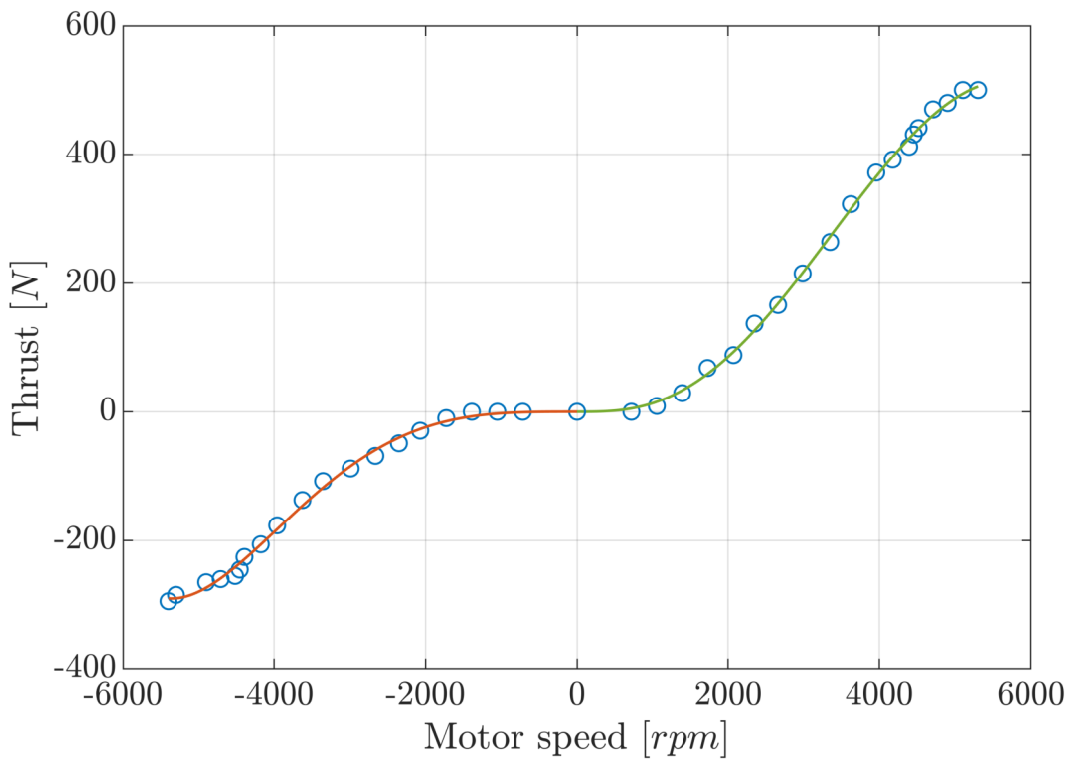


Figure 1: Motor speed and thrust for the milliAmpere ferry.

